

Dual function of rare earth carboxylate compounds on the barrier properties and active corrosion inhibition of epoxy coatings on mild steel

Yu Peng^{a,b}, Anthony E. Hughes^{b,c}, James I. Mardel^d, Glen B. Deacon^e, Peter C. Junk^f, Rainier A. Catubig^b, Maria Forsyth^b, Bruce R.W. Hinton^{b,e}, Anthony E. Somers^{b,*}

^a Key Laboratory of Optoelectronic Chemical Materials and Devices (Ministry of Education), Jiangnan University, Wuhan 430056, China

^b Institute for Frontier Materials, Deakin University, Geelong, Victoria 3220, Australia

^c CSIRO, Mineral Resources, Clayton, Victoria 3169, Australia

^d CSIRO, Manufacturing, Clayton, Victoria 3169, Australia

^e School of Chemistry, Monash University, Clayton, Victoria 3800, Australia

^f College of Science and Engineering, James Cook University, Townsville, Queensland 4811, Australia

ARTICLE INFO

Keywords:

Rare earth carboxylate
Active corrosion inhibition
EIS
Filiform corrosion
Mild steel

ABSTRACT

In this work, two rare earth carboxylate compounds, lanthanum 4-hydroxycinnamate (La(4-OHcin)₃) and yttrium 3-(4-methylbenzoyl)propanoate (Y(mbp)₃), were incorporated into bisphenol-based epoxy resin to investigate their effectiveness in coating barrier properties and active corrosion inhibition. EIS results showed that the incorporation of rare earth carboxylate inhibitors significantly improved corrosion resistance compared to the inhibitor free coating, with the global impedance modulus remaining at a level higher than 1 GΩ cm² after 219 days immersion. Following EIS experiments, cross-sectional views of the coatings exhibited a pore-plugging behavior by rare earth containing precipitates, which reinforced the coating barrier properties and delayed the electrolyte diffusion process. These effects were also reflected from the electrochemical parameters extracted from breakpoint frequency analysis and equivalent circuit modelling. Filiform corrosion experiments for artificially scratched coatings suggest that the addition of rare earth carboxylates effectively suppressed the initiation and growth of filaments as well as the development of the coating delamination front. The active corrosion inhibition is possibly related to the formation of a surface protective film consisting of bimetallic complexes and rare earth metal rich precipitates. The electrochemical measurements and surface analyses evidence the dual function of rare earth carboxylate species for enhancing coating barrier properties against electrolyte penetration and providing active corrosion inhibition for the underlying AS1020 mild steel.

1. Introduction

Chromate-based coatings have demonstrated superb corrosion protection performance for a wide variety of metals [1]. However, the use of hexavalent chromium has been strictly controlled because of its toxic and carcinogenic nature [2,3]. This has triggered studies of alternative inhibitors, including rare earth-based salts, which have been considered as promising candidates for chromate-free systems since the 1980s [4,5]. The combination of rare earth metal ions with carboxylates was proposed based on the hypothesis of a synergistic effect between each moiety of rare earth carboxylate complexes, inhibiting both the anodic and cathodic reactions of the corrosion process [6]. This was confirmed by various rare earth carboxylate inhibitors, for example cerium

salicylate (Ce(salH)₃) [7,8], lanthanum 4-nitrocinnamate (La(4-NO₂cin)₃) [9], cerium 4-methoxycinnamate (Ce(4-MeOcin)₃) [9], lanthanum 4-hydroxycinnamate (La(4-OHcin)₃) [10,11], and more recently reported praseodymium 4-hydroxycinnamate (Pr(4-OHcin)₃) [12], gadolinium 4-hydroxycinnamate (Gd(4-OHcin)₃) [13], and yttrium 3-(4-methylbenzoyl)propanoate (Y(mbp)₃) [14,15], all of which provided much better corrosion protection than their separate rare earth metal cations or carboxylate anions. The presence of the C—C double bond in the cinnamate structure and the carbonyl group of the 3-(4-methylbenzoyl)propanoate ligand also contribute to enhance the level of corrosion inhibition [16–18]. The investigation of rare earth carboxylate compounds has been an increasingly active field in chromate replacement research over the last two decades. However, most of

* Corresponding author.

E-mail address: asomers@deakin.edu.au (A.E. Somers).

<https://doi.org/10.1016/j.porgcoat.2023.107870>

Received 18 May 2023; Received in revised form 7 August 2023; Accepted 7 August 2023

Available online 18 August 2023

0300-9440/© 2023 The Authors. Published by Elsevier B.V. This is an open access article under the CC BY license (<http://creativecommons.org/licenses/by/4.0/>).

the corrosion studies for rare earth carboxylates were conducted in solutions containing dissolved inhibitors, while their effectiveness in coating systems has been less understood [19,20].

Catubig et al. [21] evaluated the effects of La(4-OHcin)_3 as a corrosion inhibiting pigment on the filiform corrosion of polyurethane coated AS1020 mild steel. They found that the addition of 10 wt% of La(4-OHcin)_3 inhibitors effectively limited the initiation and propagation of both filaments and delamination at the metal/coating interface. Vega et al. [22] studied the anticorrosion properties of different sol-gel formulations incorporated with La(4-OHcin)_3 for carbon steel, and they revealed that the addition of 5 and 10 wt% of La(4-OHcin)_3 improved corrosion resistance of sol-gel coatings and the coating defects exposed to 0.005 M NaCl solution remained pristine. The enhanced corrosion protection performance of the inhibited sol-gel coatings was hypothesized to be related to either the incorporated La(4-OHcin)_3 improved barrier properties by affecting the condensation process of sol-gel materials, thus achieving a balance between the highly cohesive polymeric network and adequate adhesion to the metal substrate, or the leached La(4-OHcin)_3 reacted with the carbon steel surface and formed a very thin and protective film [22,23]. The leaching behavior of La(4-OHcin)_3 and Y(mbp)_3 from the epoxy coating system and their active inhibition on the mild steel surface in contact with chloride contaminated environments has been investigated by Peng et al. [24]. A pH-triggered release mechanism for La(4-OHcin)_3 and Y(mbp)_3 from coatings was identified using inductively coupled plasma mass spectroscopy, and their leaching rate was also associated with the initial loading amount of inhibitor compounds. The leached La(4-OHcin)_3 and Y(mbp)_3 inhibitor species demonstrated active inhibition on mild steel surfaces by forming rare earth containing precipitates at coating defects. This is consistent with the finding that the lanthanide compounds can form insoluble hydroxides, which enable them to be used as cathodic inhibitors to mitigate corrosion of metallic alloys [25]. Apart from protecting carbon steel materials, rare earth carboxylate-based salts have also been used as inhibitor pigments for aluminum alloy [26,27]. For example, cerium tartrate containing epoxy coatings applied on AA2024-T3 exhibited a bi-functional effect, achieving both improved barrier properties and a self-healing ability when defects formed [26]. This effect was thought to be due to the release and transport of Ce ions through coatings, which reacted with OH^- to generate insoluble precipitates at coating/alloy interface.

While previous studies confirmed that the added La(4-OHcin)_3 or Y(mbp)_3 compounds could provide good coating barrier properties and active anticorrosion ability to the artificially produced defects, these experiments were usually conducted within short-term immersion (less than 100 h) at relatively low Cl ion concentrations (0.005 or 0.01 M NaCl). Moreover, the surface morphological observation for rare earth carboxylate loaded coatings focused mostly on the top view of the intact or defective coatings, while the cross-sectional views containing information of inhibitor behavior and underfilm damage were sparingly shown.

In this paper, La(4-OHcin)_3 and Y(mbp)_3 compounds were chosen as corrosion inhibiting pigments as they have been demonstrated to be highly effective on mild steel and both compatible with polymeric coatings. Thus herein, we explored their efficacy in coating barrier properties with extended immersion, together with their ability to achieve active protection when localized failure occurred. Electrochemical impedance spectroscopy (EIS) combined with breakpoint frequency analysis and equivalent circuit modelling were used to study the development of electrochemical characteristics of the inhibitor loaded coating system. To examine the active corrosion inhibition ability, filiform corrosion (FFC) tests were performed on artificially damaged coatings containing inhibitors. Coating specimens after EIS and FFC experiments were analyzed via planar and cross-sectional views using scanning electron microscopy (SEM)/energy dispersive X-ray spectroscopy (EDS), aiming to observe the structural and morphological changes of the coating system and to determine the rare earth metal distribution

within the coating matrix and on the metal substrate.

The combination of electrochemical studies and surface analyses demonstrate a dual role of rare earth carboxylates in epoxy coating system. On one hand, significantly improved coating barrier properties were achieved by a pore-plugging effect, and on the other hand, a self-healing ability was provided by forming a surface protective layer. Based on the results obtained from the above experiments a mechanism of inhibition for the incorporated rare earth carboxylate compounds is discussed.

2. Experimental

2.1. Materials

Mild steel alloy AS1020 (0.26 % C, 0.45 % Mn, 0.14 % Cr, 0.19 % Si, 0.18 % Al, 0.35 % other, Fe balance) was machined into 100 mm (L) \times 50 mm (W) \times 1 mm (H) metal panels for coating applications.

The bisphenol-based epoxy resin (Epikote 828) and an amine curing agent (Ancamine 2500) used in this work were provided by AkzoNobel Car Refinishes B.V. Lanthanum 4-hydroxycinnamate and yttrium 3-(4-methylbenzoyl)-propanoate corrosion inhibitors were prepared according to Deacon et al. [28] and de Bruin-Dickason et al. [29]. The two synthesized rare earth compounds have coordinated water, e.g. $[\text{La(4-OHcin)}_3(\text{H}_2\text{O})_5]$ and $[\text{Y(mbp)}_3(\text{H}_2\text{O})]$, but for simplicity, the inhibitor compounds are herein abbreviated without water, i.e. La(4-OHcin)_3 and Y(mbp)_3 . The chemical structure of the inhibitor anions and the polymeric structure for the coordination compounds were reported in previous work [28,29]. Silica powders (Degussa AG, 16 nm) were used as inert fillers to facilitate the dispersion of inhibitor compounds in epoxy coatings, which also improves the surface coverage and adhesion of the coatings on metal panels [30].

2.2. Sample preparations

The AS1020 mild steel panels were abraded to a P1200 grit finish using SiC paper, rinsed with distilled water, and blow dried by nitrogen gas before coating application. The La(4-OHcin)_3 or Y(mbp)_3 inhibitors (either 10 or 20 wt%) were mixed with 5 wt% of silica powders before the addition of epoxy resin and the amine hardener (epoxy resin/amine hardener (w/w) = 100/70). The mixture was subsequently ground in the mortar with a pestle until the large clumps of powders were evenly scattered in the coating matrix. The inhibitor compounds did not dissolve in the epoxy, but were rather distributed as a pigment type additive. After the mixing process, the control coatings without inhibitor compounds and the inhibited coatings containing 10 and 20 wt% of La(4-OHcin)_3 or Y(mbp)_3 complexes were applied on mild steel panels manually using a drawdown blade with a 100 μm gap. The prepared coating specimens were then placed in an oven to cure at 40 °C for 7 days. The cured coating samples were used for long-term EIS experiments and filiform corrosion tests. The average thickness for the coating without inhibitors and the coatings containing 10 and 20 wt% of La(4-OHcin)_3 or Y(mbp)_3 inhibitor powders are shown in Table 1.

2.3. Electrochemical impedance spectroscopy (EIS)

EIS experiments were applied to investigate the electrochemical

Table 1
The thickness of the coating without inhibitors and the coatings loaded with 10 and 20 wt% of La(4-OHcin)_3 or Y(mbp)_3 inhibitor particles.

Sample	Control	10 wt% La(4-OHcin)_3	10 wt% Y(mbp)_3	20 wt% La(4-OHcin)_3	20 wt% Y(mbp)_3
Thickness (μm)	237.9 \pm 25.6	233.9 \pm 27.6	227.8 \pm 24.3	246.6 \pm 28.8	252.9 \pm 25.8

characteristics for the reference coatings without inhibitors and 10 wt% of La(4-OHcin)₃ or Y(mbp)₃ incorporated coatings immersed in 1 M NaCl solution for 219 days (the duration of immersion was determined to allow sufficient degree of coating degradation, while still allow the discrimination of inhibitor effectiveness). It is worth noting that all the coating specimens were transferred to an oven set at 40 °C between 86 and 92 days of immersion, aiming to accelerate electrolyte penetration into coatings. EIS measurements were carried out using a three-electrode setup, comprising the coated mild steel panel as working electrode with a surface area of 7.1 cm², a saturated Ag/AgCl reference electrode, and a titanium mesh counter electrode. The electrochemical experiments were conducted in a Faraday cage using BioLogic VMP3 potentiostat controlled by EC-Lab software. EIS tests were performed at open circuit potential (OCP) over a frequency range from 30 kHz to 10 mHz with 6 data points per decade and a sinusoidal perturbation of 15 mV. The impedance responses were monitored on two different test areas of one coated panel for each coating system. Coatings with and without inhibitors were later removed and sectioned for SEM/EDS analysis.

2.4. Breakpoint frequency method

Breakpoint frequency (f_b) in the Bode magnitude plot represents the boundary where a capacitive region (slope equals -1) first transitions to a resistive region (slope equals 0) when the frequency shifts from high to low range and represents the level of coating delamination [31,32]. At the transition, the impedance of the capacitance is equal to the plateau resistance and the phase angle is approximately 45° [33]. Therefore, when the phase angle first shifts below 45°, following the curve from higher to lower frequencies, the corresponding frequency can also be determined as f_b in the Bode phase angle plot [32]. The benefit of using the breakpoint frequency method is to quickly assess the coating delamination behavior when combining with OCP values and impedance data. Initially, where there is no defect area, a breakpoint frequency may not be detected. Some electrolyte penetration will eventually occur, and the coating will begin to detach, following which a breakpoint frequency will be detected. A measured breakpoint below 10 Hz, is termed a low breakpoint frequency (f_l). As the coating continues to delaminate, it enters what has been termed the incubation period, between 10 and 100 Hz. Once delamination becomes significant breakpoint frequencies are detected above 100 Hz and termed the high breakpoint frequency (f_h), which represents the region of significant and increasing delamination as f_b increases [31]. Thus, a f_b in the region below 10 Hz is indicative of a protective coating with a very small defect area and a value above 100 Hz implies significant coating delamination processes, with the incubation stage defined in the frequency region between 10 and 100 Hz [33].

2.5. Filiform corrosion tests

The control coatings without inhibitors and the inhibited coatings loaded with 10 and 20 wt% of La(4-OHcin)₃ or Y(mbp)₃ compounds were applied on mild steel panels using the method described in Section 2.2. A 10 mm length slot was artificially scribed at the center of each coating specimen using a scalpel blade. The newly scribed defect was then exposed to concentrated HCl acid vapor (32 %) according to the specification DIN65472 for 15 min to initiate corrosion [30]. After HCl corrosion activation, the coated mild steel panels with defects were vertically placed in a sealed container with two beakers of saturated KCl. Subsequently, the container was transferred to an oven at 40 ± 2 °C to create an atmosphere of 85 % relative humidity. The initiation and growth of filiform corrosion surrounding the artificially scratched coating were recorded at regular intervals for up to 30 days using optical microscopy (Leica MZ-6 microscope with LAS V4.0 software). Coatings were later removed using acetone for the SEM/EDS analysis of the underlying metal substrate.

2.6. Scanning electron microscopy (SEM) and energy dispersive X-ray spectroscopy (EDS)

For the specimens after EIS experiments and filiform corrosion tests, a JEOL JSM-IT300LV SEM attached with an Oxford 50 mm² X-Max^N silicon drift EDS detector was used under a beam accelerating voltage of 15 kV to analyze the morphological and chemical information for the coating matrix and steel surface via planar and cross-sectional views. All the sample surfaces were coated by a thin layer of carbon (Polaron SC7610 sputter coater with CA7615 carbon accessory) to improve the conductivity under 15 kV accelerating voltage.

3. Results

3.1. EIS measurements

EIS measurements were carried out on two different test areas for the control coatings without inhibitors and the inhibited coatings modified with 10 wt% of La(4-OHcin)₃ or Y(mbp)₃ particles (an example for the position of the coating specimen undergoing an EIS experiment is shown in Fig. S1 in SI), named as Control (1) and (2), La (1) and (2), and Y (1) and (2), respectively. In order to facilitate the reading of EIS results, the development of the total impedance at 0.01 Hz ($Z_{0.01\text{Hz}}$) is shown in Fig. 1a. $Z_{0.01\text{Hz}}$ data was chosen for the comparison of different coating specimens as this frequency highlights the corrosion or protection activities at the metal/coating interface. Fig. 1a shows that the initial $Z_{0.01\text{Hz}}$ values for each sample were scattered and the trend became more pronounced after 92 d of immersion, i.e., after the acceleration process. Moreover, bigger difference in $Z_{0.01\text{Hz}}$ values were observed between the two test areas of the inhibitor coated systems in comparison with the control specimen. This phenomenon clearly shows that direct addition of inhibitor pigments to the epoxy resin may cause highly scattered and uncontrolled impedance responses, resulting from the already existing flaws during coating preparation process (affected by coating thickness, particle agglomeration, and/or air bubbles). Fig. 1a confirms that the initial coating properties could significantly affect the long-term corrosion protection performance of the coated specimens.

In Fig. 1b the variation of the $Z_{0.01\text{Hz}}$ values for a given time to the first measurement (i.e. Z_t/Z_1) was plotted against immersion time, which was used to filter out the possible influence of the initial coating properties. The normalizing of the impedance to the initial measurement (Fig. 1b) shows that the Y (2), La (1) and Control (2) specimens exhibited less impedance variation at 0.01 Hz over time, in particular, after the acceleration process in comparison with their counterparts. These results indicate that the initial coating properties of Y (2), La (1), and Control (2) specimens were more robust, thus their impedance instabilities with time were more likely to be linked with the changes of inhibitor behavior and coating barrier properties rather than the pre-existing flaws and defects in coatings before immersion started. Therefore, the Y (2), La (1), and Control (2) coating specimens were chosen to investigate the evolution of electrochemical characteristics and to link these with the inhibitor behavior and the changes of coating barrier properties. The EIS results for the Y (1), La (2), and Control (1) coating specimens were presented in Fig. S2 in SI.

Fig. 2 shows the representative EIS Bode plots for the control and the inhibited coating specimens during long-term immersion. Fig. 2a shows that the total impedance for the control coating decreased by almost two orders of magnitude over 219 days immersion. The reduction of impedance modulus suggests the presence of inner pathways in coatings, which facilitate the penetration of electrolyte toward the metal surface [34]. The phase angle plot (Fig. 2b) shows that the time constant at the high frequency region, describing the capacitive behavior, also narrowed and decreased with increasing time, indicating the gradual deterioration of the coating barrier properties of the control specimen. Moreover, the formation of a new time constant in the medium frequency range after 180 days immersion, as shown in Fig. 2b, suggests

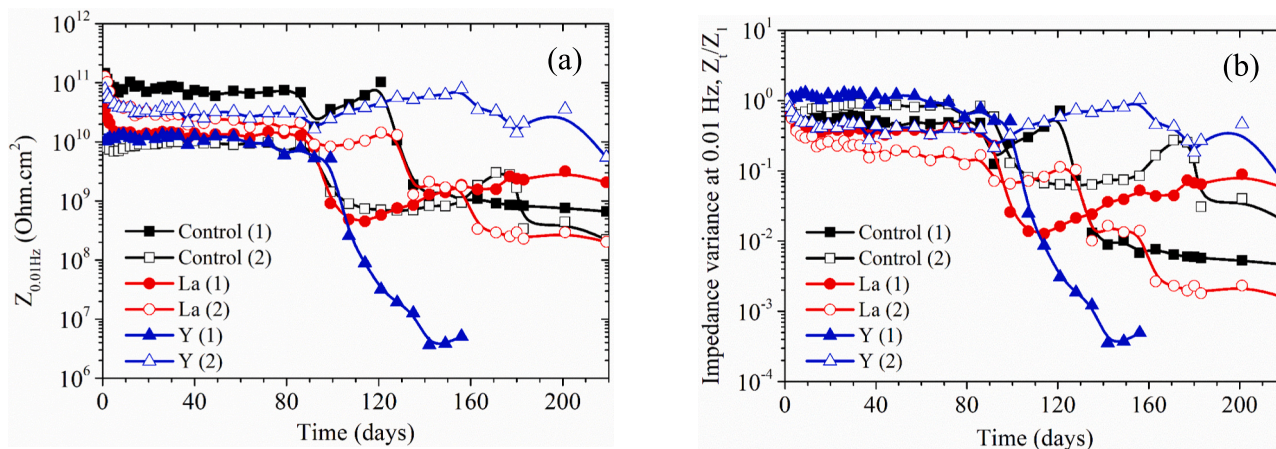


Fig. 1. Development of the total impedance (a) and impedance variance (b) for the coatings without inhibitors (Control (1) and Control (2)) and the 10 wt% of La(4-OHcin)₃ loaded coatings (La (1) and La (2)) as well as the coatings containing 10 wt% of Y(mbp)₃ inhibitors (Y(1) and Y(2)) during 219 days immersion in 1 M NaCl.

the occurrence of corrosion product films [35]. For the coating specimen loaded with 10 wt% La(4-OHcin)₃, Fig. 2c exhibits a high level of total impedance (during the early 92 days immersion) before the value significantly decayed by approximately one order of magnitude (after 128 days immersion), which was followed by a trend of restoration and the impedance curves remained stable until the end of immersion. The corresponding phase angle values (Fig. 2d) also reduced and recovered as immersion time increased, while no additional time constant was observed in the middle frequency region compared to the control specimen. Fig. 2d shows that a low frequency time constant was observed in 1 d and 49 d EIS spectra, but with the increase of immersion time, the time constant at low frequencies became undetected. In the early stage of immersion, the detection of a low frequency time constant is associated with the corrosion process on the coated metal surface. With the immersion time further increased, the incorporated inhibitor particles dissolved and released with the electrolyte penetration process, which could form a thin surface film to suppress corrosion on the metal substrate. Therefore, the low frequency time constant was not evident in EIS spectra after the longer term of immersion. The 10 wt% Y(mbp)₃ containing specimen (Fig. 2e and f) shows a gradually decreasing trend for both overall impedance modulus and phase angle values during the testing period. While the impedance spectra and the accompanied phase angle curve increased after 128 days immersion, the extent of this decay and recovery effect was minor compared with that observed for the La(4-OHcin)₃ counterpart. At the end of EIS tests, the inhibitor loaded coating systems show a higher global impedance modulus at low frequencies and a broader plateau of phase angle at high frequencies, together with the absence of a medium frequency time constant compared to the non-inhibited coating specimen. This demonstrates that the addition of 10 wt% of inhibitor particles reinforces the coating barrier properties and the corrosion resistance at the metal/coating interface.

To further compare the coating properties of the control and the inhibited specimens, parameters such as impedance at 0.01 Hz ($Z_{0.01\text{Hz}}$), open circuit potential (OCP), and breakpoint frequency (f_b) were determined after EIS measurements. The development of $Z_{0.01\text{Hz}}$ with time was chosen as the total impedance at 0.01 Hz highlights the ongoing corrosion or protection phenomena that occurs at the metal surface [36,37] and OCP time evolution also reveals coating properties and other underfilm corrosion processes [38,39]. The f_b extracted from Bode phase angle plots was used to evaluate the coating degradation behavior, which shifts to higher frequencies as delamination increases [33]. The evolution of f_b , OCP, and $Z_{0.01\text{Hz}}$ parameters with time obtained for the control coating and the inhibited coating are depicted in Fig. 3a–f. The boundary of the maximum low breakpoint frequency (f_l) is set at 10 Hz and the minimum value for the high breakpoint frequency

(f_h) is determined at 100 Hz, with the incubation stage of coating degradation defined in the frequency range between 10 and 100 Hz [31].

Fig. 3a shows that the f_b for non-inhibited coating rapidly shifted to the incubation stage before f_h was apparently observed after 99 days immersion. The appearance of clear f_h corresponded to the sharp decline of $Z_{0.01\text{Hz}}$ and OCP values by one order of magnitude and 100 mV, respectively (Fig. 3b). This indicates the deterioration of coating barrier properties with time. The $Z_{0.01\text{Hz}}$ gradually increased from 7×10^8 to $3 \times 10^9 \Omega \text{ cm}^2$ between 120 and 180 days immersion, resulting from the additional resistance provided by the corrosion products formed on the metal surface. At the end of immersion, the $Z_{0.01\text{Hz}}$ value for the control coating decreased considerably to around $2 \times 10^8 \Omega \text{ cm}^2$. For the coating modified with La(4-OHcin)₃ inhibitor, the f_l quickly increased and reached a plateau close to 0.5 Hz in the early stage of immersion, as shown in Fig. 3c. After the acceleration process between 86 and 92 days immersion, the f_b shifted to higher values and entered the incubation stage before the value rapidly dropped back to the f_l region, ending up at around 2 Hz. Fig. 3d shows that the OCP and $Z_{0.01\text{Hz}}$ remained relatively stable at a high level, which suggests good coating shielding effect and corresponded to the plateau of f_l observed in Fig. 3c before the acceleration process. The sharp increase of f_b into the incubation stage (Fig. 3c) can be linked with the significant decay of both the OCP and $Z_{0.01\text{Hz}}$ by 550 mV and one order of magnitude, respectively (Fig. 3d). Subsequently, the OCP for the La(4-OHcin)₃ loaded coating slightly fluctuated at around -500 mV to the end of the EIS experiments, while the corresponding $Z_{0.01\text{Hz}}$ values gradually increased from about 4×10^8 to $2 \times 10^9 \Omega \text{ cm}^2$ with time. Fig. 3e shows that the f_b data remained below 1 Hz for the coating containing Y(mbp)₃ throughout the immersion, indicating that only minimal deterioration of the coating barrier properties occurred during the entire experiments. The $Z_{0.01\text{Hz}}$ data for the Y(mbp)₃ specimen maintained above $10^{10} \Omega \text{ cm}^2$ over nearly 200 days immersion before the value ended up at around $5 \times 10^9 \Omega \text{ cm}^2$ (Fig. 3f). The corresponding OCP values (Fig. 3f) stabilized around -100 mV for the majority of immersion time except that a dramatic shift of OCP to positive values between 160 and 183 days immersion. For the inhibitor loaded coatings, the absence of f_h and the development of OCP and $Z_{0.01\text{Hz}}$ confirms the mitigation of coating degradation and underfilm corrosion processes.

Two equivalent circuit (ECs), EC 1 and EC 2 (shown in Fig. 4), were used to fit the EIS spectra for the coating specimens during long-term immersion. EC 1 is commonly used for a coated metal substrate and is applicable to fit the EIS data for the coating samples before 92 days immersion. Subsequently, the model converts to EC 2 for the fitting of EIS data due to the spectra began to change after the acceleration process (between 86 and 92 days immersion) and new time constant

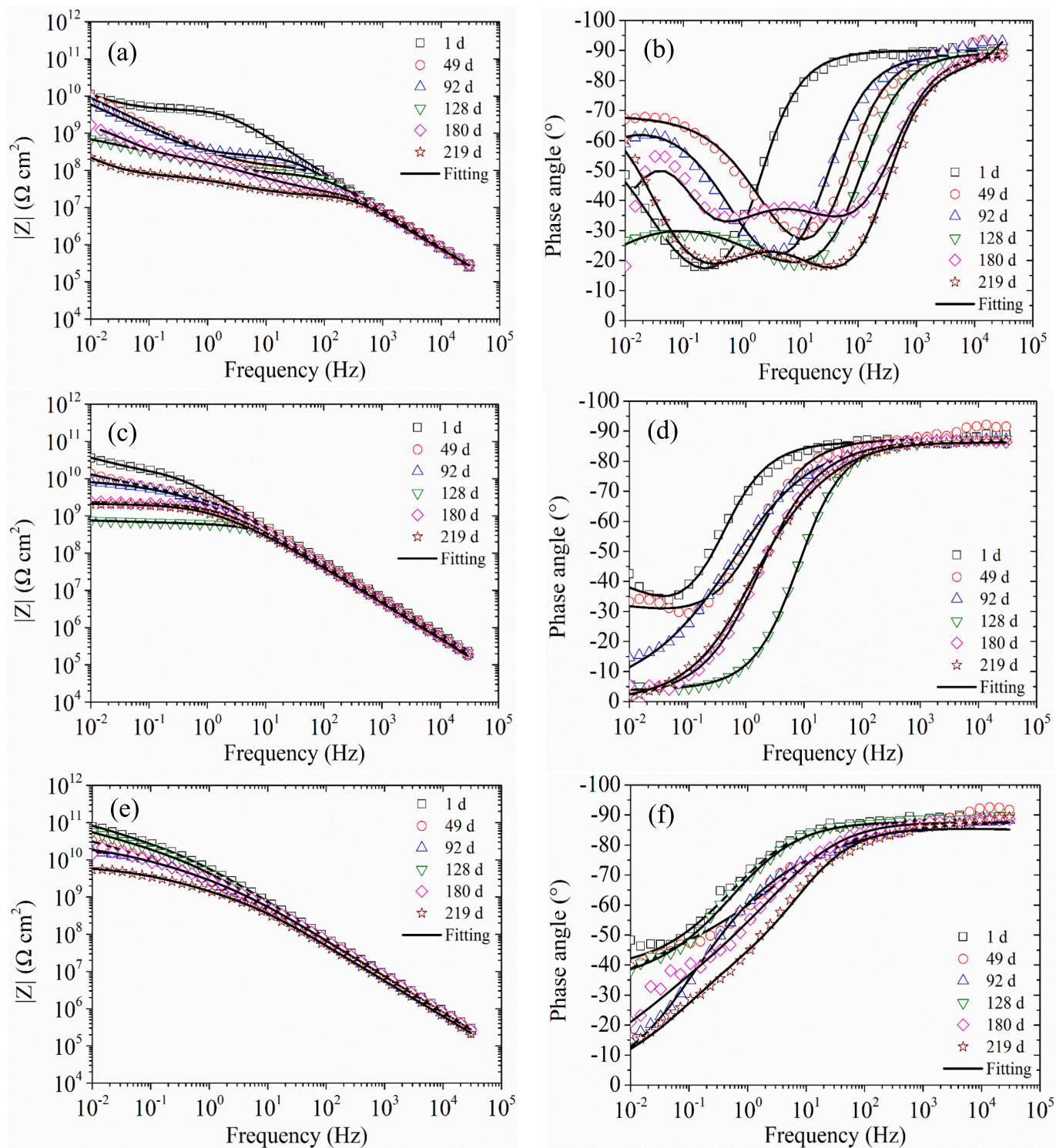


Fig. 2. Bode impedance modulus and phase angle plots for the coated mild steel panels during 219 days immersion in 1 M NaCl: (a and b) reference coating and (c and d) coating loaded with 10 wt% $\text{La}(4\text{-OHcin})_3$ and (e and f) coating containing 10 wt% $\text{Y}(\text{mbp})_3$.

appeared at lower frequencies, as shown in Fig. 2.

In the EC 1 and EC 2, R_s for the solution resistance, and CPE_{coat} and R_{coat} represent the constant phase element (CPE) for the capacitance of the coating system and the corresponding coating pore resistance. CPE_{ox} and R_{ox} describe the contribution of the formed oxide layer on the metal surface, and CPE_{dl} and R_{ct} are used to depict the double layer capacitance and the charge transfer resistance at the metal/oxide interface [40]. In this work, CPE is used to represent the non-ideal capacitive

behavior resulting from surface inhomogeneity created by the released inhibitor species and the corrosion products.

The development of R_{coat} , CPE_{coat} , R_{ox} , CPE_{ox} , R_{ct} , and CPE_{dl} values with immersion time for the control coating and the coating loaded with 10 wt% of $\text{La}(4\text{-OHcin})_3$ or $\text{Y}(\text{mbp})_3$ inhibitor particles were extracted and compared based on the results of fitting using EC 1 and EC 2 (shown in Fig. 5).

Fig. 5a shows the evolution of R_{coat} values with immersion time for

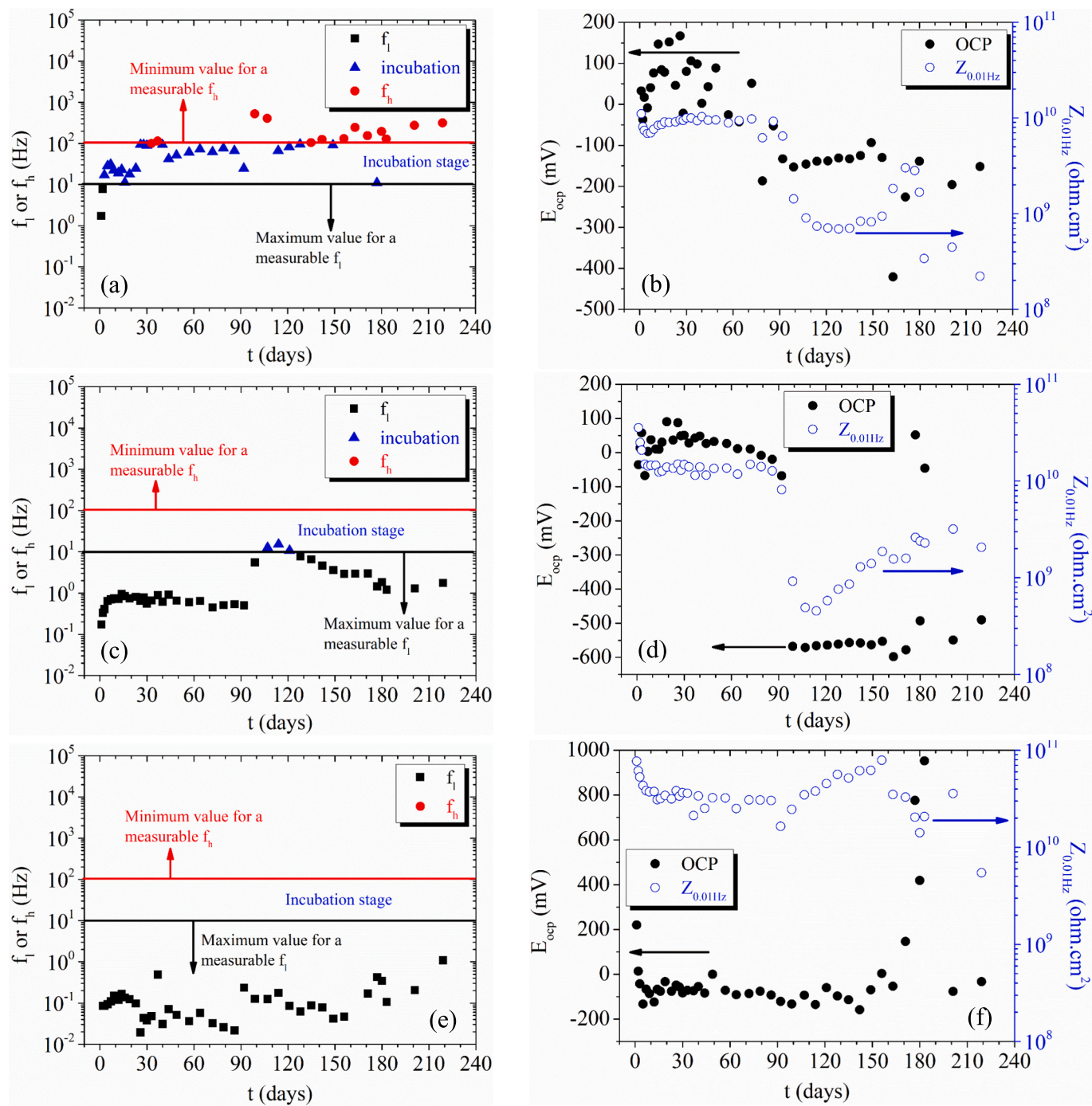


Fig. 3. Evolution of breakpoint frequency f_i or f_h and OCP and $Z_{0.01\text{Hz}}$ values with immersion time for the non-inhibited coating (a and b) and 10 wt% of La(4-OHcin)₃ (c and d) or Y(mbp)₃ (e and f) incorporated coating. The measurable boundaries for f_h and f_i are outlined using red and black horizontal lines, and the area in between represent the incubation stage. (For interpretation of the references to color in this figure legend, the reader is referred to the web version of this article.)

the three coating systems. The R_{coat} values for the control coating presents a gradually decreasing trend with time, and the value reached $1.8 \times 10^7 \Omega \text{ cm}^2$ at the end of the experiment. The inhibitor loaded coatings exhibit highly fluctuated R_{coat} , particularly after the acceleration process, which could be associated with the competition between water uptake and inhibitor response. The water uptake induced the dissolution and leaching of inhibitors, creating voids and pores in the coating matrix, which in turn further accelerated electrolyte penetration and degraded coating barrier properties, resulting in the sharp decline of R_{coat} . The rise and recovery of R_{coat} values might be attributed to the re-precipitation of inhibitor species in the pores and pathways when the

concentration of the released inhibitors exceeded their solubility limit. At the end of the EIS experiments, the R_{coat} value for the La(4-OHcin)₃ loaded coating and the Y(mbp)₃ loaded coating located at $6.2 \times 10^8 \Omega \text{ cm}^2$ and $1.8 \times 10^8 \Omega \text{ cm}^2$, respectively. The corresponding CPE_{coat} values for the control coating and the coating loaded with inhibitors slightly varied within the range between 1.0 and $6.0 \times 10^{-11} \text{ F s}^{n-1} \text{ cm}^{-2}$ throughout the experiments, as shown in Fig. 5b. This phenomenon implies that the added inhibitor particles are compatible with the epoxy matrix [41]. The higher CPE_{coat} values obtained for the coating containing La(4-OHcin)₃ can be linked to the higher solubility limit and the faster leaching rate of La(4-OHcin)₃ species [24], which leads to a

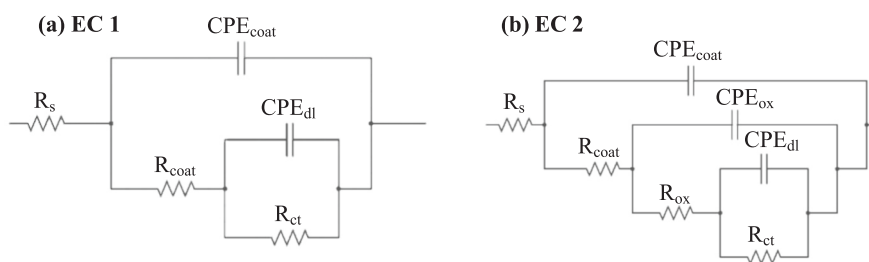


Fig. 4. Equivalent circuit model used to fit EIS data for the control coating and the inhibitor loaded coating applied on mild steel during 219 days of immersion in 1 M NaCl solution: (a) EC 1 is applied to the coating specimens before 92 days immersion; (b) EC 2 is used for the fitting of EIS data for the coating specimens after 92 days immersion.

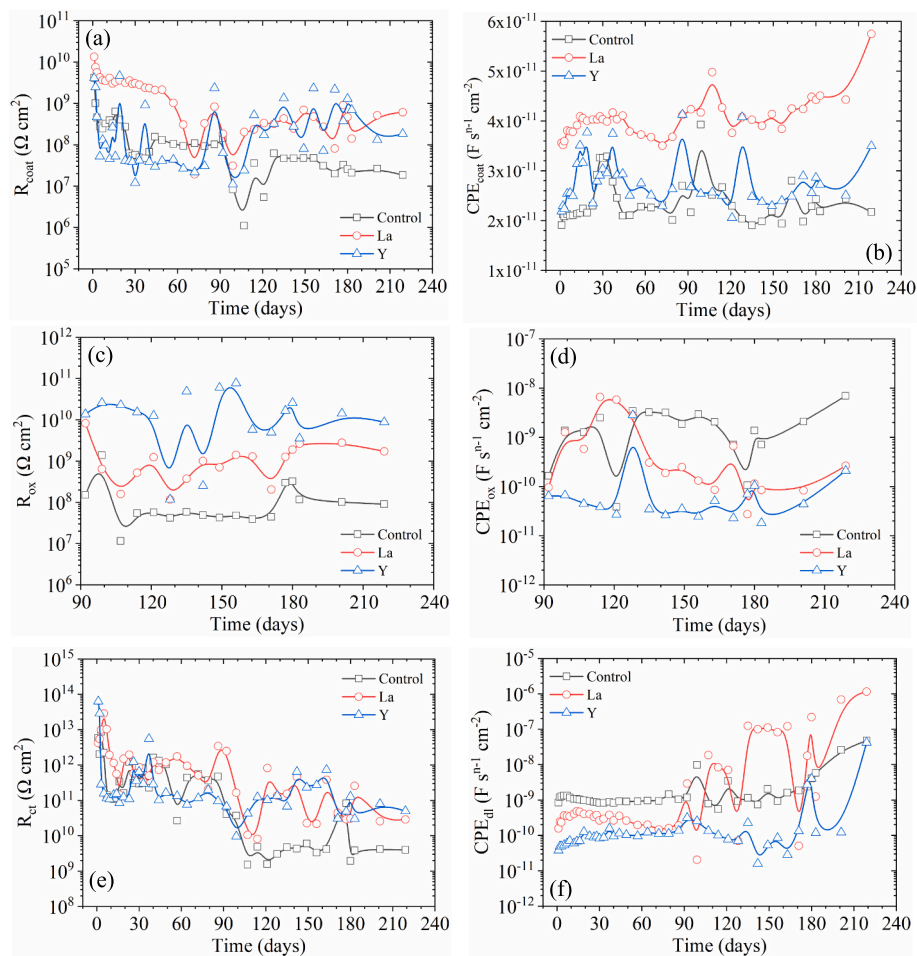


Fig. 5. The development of (a) R_{coat} , (b) CPE_{coat} , (c) R_{ox} , (d) CPE_{ox} , (e) R_{ct} , and (f) CPE_{dl} for the control coating without inhibitor additives and the coating incorporated with 10 wt% of La(4-OHcin)_3 or Y(mbp)_3 particles immersed in 1 M NaCl solution as a function of time. The smoothed lines were obtained using B-Spline fit.

greater effect in the coating barrier properties. Fig. 5c and d show the evolution and scatter of the resistance and capacitance of the formed oxide layer (R_{ox} and CPE_{ox}) on the metal surface as a function of immersion time. Fig. 5c shows that the R_{ox} obtained from coatings loaded with inhibitors consistently remained at higher values compared to that of the control coating. At the end of experiments, the R_{ox} increased by a factor 20 for the La(4-OHcin)_3 loaded coating and a factor 100 for the Y(mbp)_3 loaded coating in comparison with the coating without inhibitor. This indicates that a more robust oxide layer was formed on the metal surface by the released inhibitor species. Moreover, the R_{ox} values for the inhibitor loaded coatings became fluctuated over time, which possibly implies the breakdown and repair of the protective surface film

[42]. The development of CPE_{ox} with immersion time for each coating system is presented in Fig. 5d. It can be observed that the CPE_{ox} of the control coating rapidly increased and remained at higher values compared to those of the inhibitor loaded coatings after 92 days immersion. This suggests that the corrosion products were less resistant for the coating without inhibitor, resulting in rapid degradation of this oxide layer. The CPE_{ox} of the Y(mbp)_3 loaded coating remained relatively stable at a low level within most of the time. The La(4-OHcin)_3 loaded coating exhibits a dramatic increase of CPE_{ox} between 90 and 120 days immersion before the value gradually reverted to a similar level compared to its Y(mbp)_3 counterpart. At the end of experiments, the CPE_{ox} values for coatings incorporated with inhibitors were reduced

by a factor 30 lower compared to the control coating, suggesting that a protective layer was formed on the metal surface. The corrosion process at the metal/oxide interface can be characterized by the time constant consisting of the R_{ct} and the CPE_{dl} . Fig. 5e and f show the development of the R_{ct} and CPE_{dl} during the long-term immersion. Compared to the control coating specimen, both the inhibitor loaded coatings obtained larger R_{ct} values over time (Fig. 5e), indicating improved corrosion protective properties of the formed oxide layer. It is worth noting that, during the entire immersion, the trend of gradually decreasing R_{ct} (Fig. 5e) and increasing CPE_{dl} (Fig. 5f) for all the coating systems indicates that corrosion activity still occurred underneath the oxide layer.

The fitting results of EIS data (Fig. 5) show that the R_{coat} , R_{ox} and R_{ct} values of the inhibited coatings were considerably enhanced at the end

of immersion compared to the control coating. The oscillations of R_{coat} , R_{ox} and R_{ct} values were consistent with the decline and restoration of the impedance modulus and phase angle curves obtained for the coatings incorporated with rare earth carboxylate inhibitors (Fig. 2).

3.2. SEM/EDS analysis

3.2.1. Planar view of coatings

The pristine surface morphology of the as-prepared coating samples (before long-term immersion) is shown in Fig. S3 in SI. Fig. S3 reveals that the inhibitor loaded coating systems contain some typical characteristics, such as (a) isolated inhibitor particles with a rod-like structure, (b) agglomerated inhibitor clusters, and (c) the presence of voids. SEM/

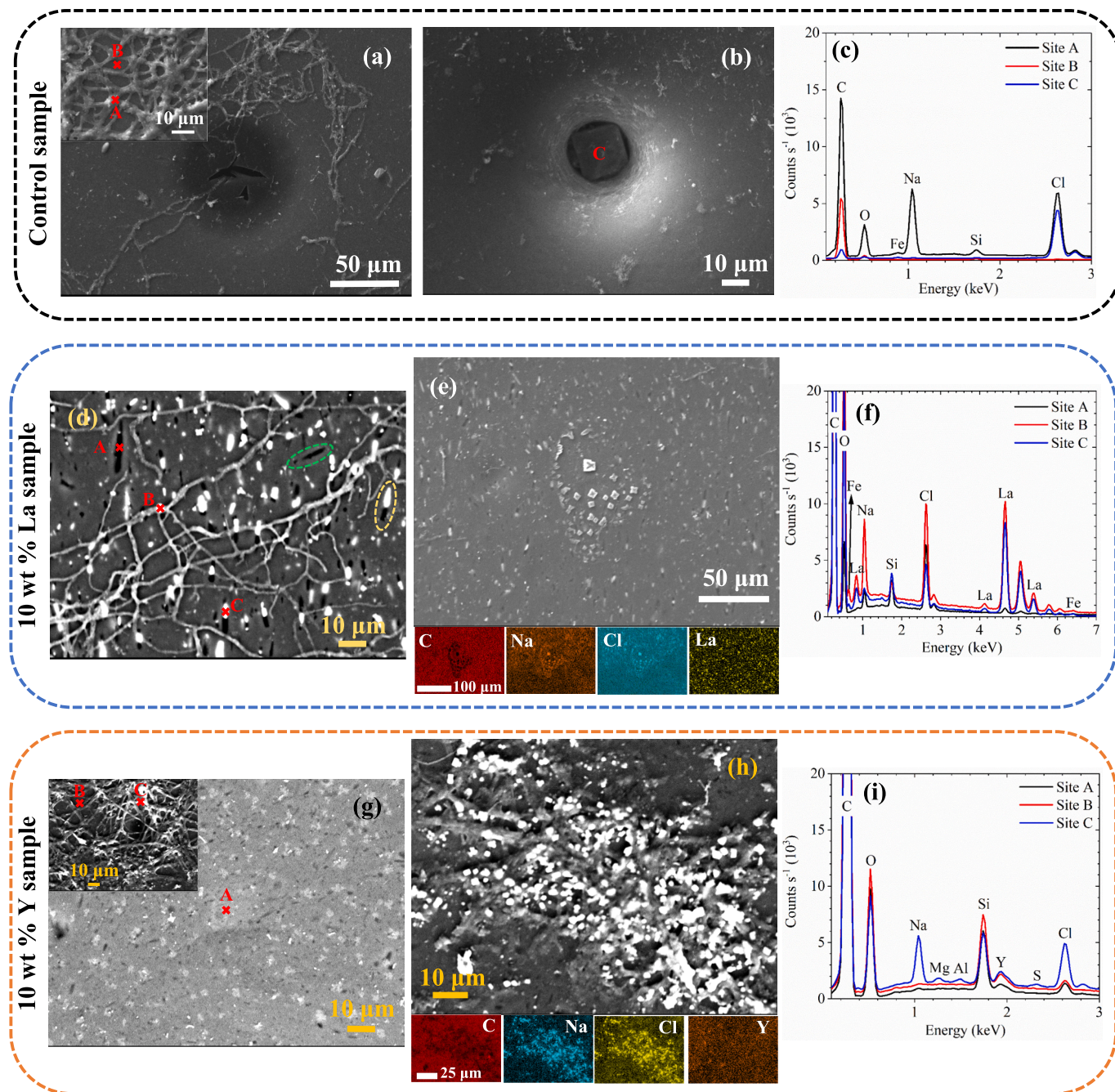


Fig. 6. The surface analysis via planar view for the reference coating (a, b, and c), the 10 wt% of La(4-OHcin)_3 loaded coating (d, e, and f), and the coating containing 10 wt% of Y(mbp)_3 (g, h, and i) after long-term EIS experiments. (For interpretation of the references to color in this figure, the reader is referred to the web version of this article.)

EDS analysis was employed to examine the surfaces of the control coating and the inhibitor loaded coatings after long-term EIS experiments. Fig. 6 shows that some common features, for instance, the fiber-shaped structure and the salt deposition were observed on all the coating surfaces. The fiber network is thin (shown in Fig. 6d and the inserted SEM images in Fig. 6a and g) and might represent the degradation of the skin layer, which typically forms just at the surface of the polymer matrix [43]. EDS spectra confirm the presence of Na and Cl on the fiber-like network (site A in Fig. 6a, site B in Fig. 6d, and site C in Fig. 6g), which could be associated with the ingress of electrolyte into the epoxy matrix. This infiltration process can be inferred from the salt deposition in coating defects, as presented in Fig. 6b, e and h.

For the surface of the $\text{La}(\text{4-OHcin})_3$ loaded coating after long-term immersion, Fig. 6d shows that numerous bright particles and voids with different sizes and shapes were present surrounding the fiber-shaped network. It can be noted that some rod-shaped voids were formed in the coating (a representative site was highlighted by green oval in Fig. 6d), suggesting that the incorporated $\text{La}(\text{4-OHcin})_3$ particles were completely dissolved and leached out from those sites. Moreover, some voids were observed to be partially blocked by insoluble precipitates, as shown in Fig. 6d, where a typical site has been marked using a yellow oval. EDS analysis (Fig. 6f) confirms the presence of La on the bright particles located at the fiber network (site B in Fig. 6d) and in the half-blocked voids (site C in Fig. 6d), while the signal intensity of La was nearly negligible in the empty voids created by the released inhibitors

(site A in Fig. 6d). Also, it is worth noting that the precipitates remaining in the half-blocked voids comprised a large amount of La to around 30 wt% (Fig. S4 in SI), which was significantly higher than that of detected for the as-prepared $\text{La}(\text{4-OHcin})_3$ containing coating (only about 11 wt% of La detected on the incorporated inhibitor particles, see Fig. S5 in SI). This indicates that the remaining particles observed in the partially blocked voids were less likely to be the unreacted $\text{La}(\text{4-OHcin})_3$ inhibitors, which implies a complex behavior of the incorporated inhibitors during electrolyte penetration process.

The top surface of the $\text{Y}(\text{mbp})_3$ containing coating after immersion exhibits a number of isolated particle clusters and voids, as shown in Fig. 6g. Fig. 6i shows that Y and Cl were detected from the particle clusters (site A in Fig. 6g), the epoxy matrix (site B in Fig. 6g), and the exposed fiber structure (site C in Fig. 6g). The feature of scattered particle islands was not observed for the as-prepared coating modified with $\text{Y}(\text{mbp})_3$ (Fig. S6 in SI), suggesting that the formation of this characteristic is correlated to the movement of inhibitor species and the ingress of Cl^- ions into coatings.

3.2.2. Cross-sectional view of coatings

The coating was peeled from the metal substrate and subsequently sectioned using a microtome without further mechanical polishing, aiming to examine the inhibitor behavior in coatings via a cross-sectional view.

A portion of the control coating was removed from the steel substrate

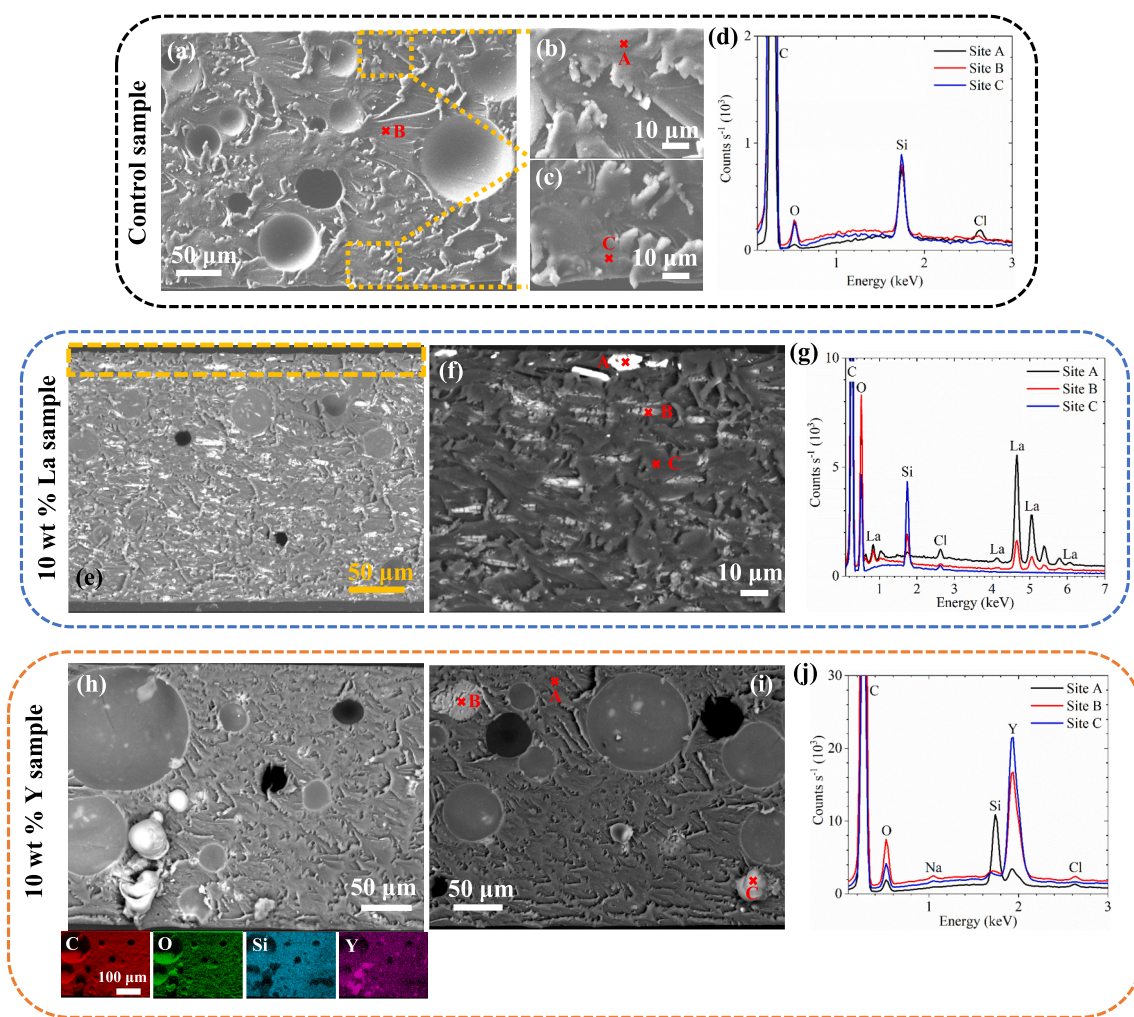


Fig. 7. The surface analysis via cross-sectional view for the reference coating (a, b, c and d), the 10 wt% of $\text{La}(\text{4-OHcin})_3$ loaded coating (e, f, and g), and the coating containing 10 wt% of $\text{Y}(\text{mbp})_3$ (h, i, and j) after long-term EIS experiments. (For interpretation of the references to color in this figure, the reader is referred to the web version of this article.)

and the typical surface morphology for the sectioned coating surface is displayed in Fig. 7a, b, and c. Fig. 7a shows that the sectioned surface for the control coating remained intact without apparent defects or damages observed at the top and the bottom surfaces, as shown by the enlarged images in Fig. 7b and c. However, corrosion attacks did occur as the presence of defects on the top coating surface (shown in Fig. 6a) and the observation of pitting spots on the steel substrate underneath (shown in Fig. 8a). This indicates that the electrolyte pathways in coatings were tortuous, which makes it difficult to capture the route via 2D SEM imaging. EDS results for the sectioned surface (Fig. 7d) show that very limited Cl was detected from the top surface (site A), while Cl was absent from the middle and bottom surfaces (site B and site C).

Fig. 7e shows the fractured surface of the La(4-OHcin)_3 loaded

coating after long-term EIS experiments. The bright rod-shaped particles represent the La containing species and the grey area denotes the polymer matrix. The planar view of the coating loaded with La(4-OHcin)_3 (Fig. 6d) shows some voids and half-blocked pores present in the vicinity of the top surface. Also, a previous study for the same coating system confirms that the leaching of inhibitors predominantly occurred at the surface in proximity to the coating/solution interface [24]. Therefore, the area close to the top surface of the sectioned coating (see the yellow rectangle in Fig. 7e as an example) has been navigated to examine the inhibitor behavior in coatings during long-term immersion. Fig. 7f shows that the region near the coating/solution interface exhibits three different brightness, which consists of the very bright particle clusters located close to the top surface (site A), the grey species

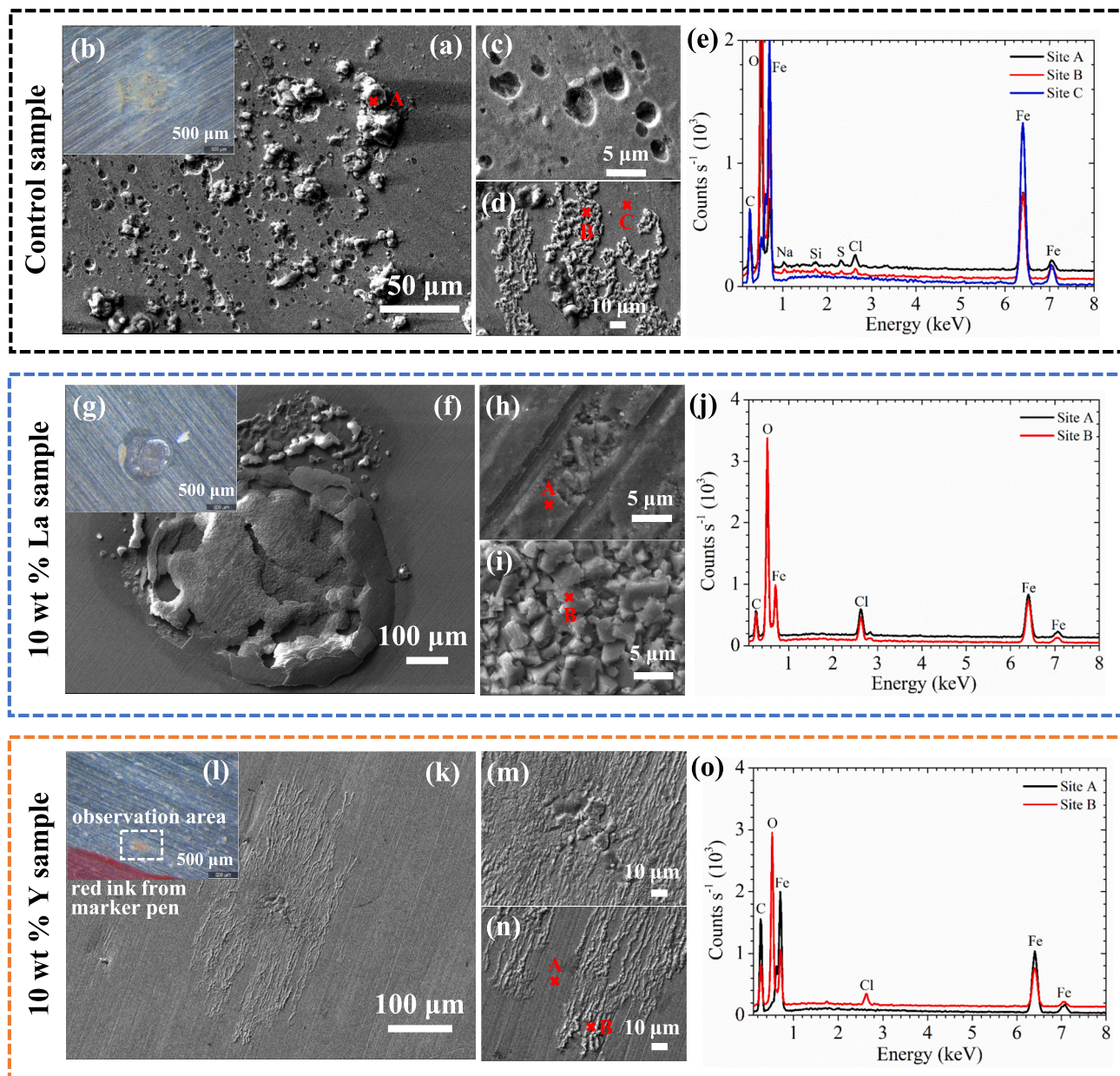


Fig. 8. Mild steel surface analysis for the reference specimen after long-term immersion: (a) SEM and (b) optical microscopy images for the overall corroded area; SEM images for the region of (c) pitting and (d) filiform corrosion; (e) EDS spectrum on the corrosion products (site A), the filaments (site B), and the metal surface (site C). Mild steel surface observation for the 10 wt% of La(4-OHcin)_3 loaded specimen after long-term immersion: (f) SEM and (g) optical microscopy images for the overall rusted area; SEM images for the central area of the blister corrosion products with (h) polishing scratches and (i) small lumps; (j) EDS spectrum on the site close to the polishing marks (site A) and on the lumps (site B). Mild steel surface analysis for the 10 wt% of Y(mbp)_3 loaded sample after long-term immersion: (k) SEM and (l) optical microscopy images for the entire corroded region; Images (m) and (n) to show the amplification of the middle part and the boundary of the filiform corrosion products, respectively; (o) EDS spectrum for the metal surface (site A) and the filaments (site B).

observed in the bulk of the coating (site B), and the dark region representing the polymer matrix surrounding those particles (site C). A considerably higher amount of La was detected from the very bright particle clusters compared to the grey species, which can be implied by the corresponding signal intensity of La from site A and site B shown in Fig. 7g. The grey species were formed due to the dissolution and release of La(4-OHcin)₃ inhibitor particles during the water uptake process, resulting in the formation of electrolyte pathways in coatings. The presence of the very bright particle clusters could be correlated with the agglomeration and re-precipitation of the La containing species when the concentration of the released inhibitors exceeded their solubility limits in the coating channels.

Fig. 7h and i shows that the sectioned Y(mbp)₃ containing coating displays a unique characteristic, that is the presence of some protuberant nodules on the surface in comparison with its La(4-OHcin)₃ counterpart. Generally, the nodules were observed at deeper sites toward the coating/metal interface, suggesting a deeper penetration depth of electrolyte into coating matrix. EDS mapping shown in Fig. 7h confirms the presence of Y in the nodules. Fig. 7i shows that a flattened cluster of particles (site B) and a nodular structure (site C) were present on the sectioned coating surface, while no particularly bright particles were observed from the top area (site A). EDS spectra (Fig. 7j) show that higher signal intensity of Y was detected from the nodule than the particle cluster, and trace amount of Cl was present in all the three sites. The reason that these nodules may only be seen in the deeper clusters is that the ones nearer the upper surface may have dried out before the sectioning process. The formation of nodules could be associated with the dissolution and diffusion of Y(mbp)₃ species combined with the electrolyte penetration through the channels in coatings, producing a gel-like speciation in the pathways and explaining why they were not seen on the samples before immersion (Fig. S7 in SI). In the vacuum condition created for carbon coating process and/or SEM observation, the gel-like species were sucked out on the sectioned surface to form nodular precipitates.

The combination of the planar and cross-sectional SEM/EDS analysis exhibits different inhibitor behavior between La(4-OHcin)₃ and Y(mbp)₃ compounds in coatings. In the early stage of immersion, the water-uptake process triggered the dissolution and leaching of inhibitor compounds, resulting in the formation of voids in coatings. This process corresponded to the decrease of the total impedance modulus and the contraction of the phase angle plateau (Fig. 2). The released inhibitor species were thought to diffuse through the interconnected networks created by the dissolved inhibitor particles [44]. The local concentration of inhibitor species in the channels was continuously increased until it surpassed the solubility limit, which led to the precipitation of insoluble particle agglomerates in the pathways. This pore-plugging effect was observed from the La(4-OHcin)₃ loaded coating (Figs. 6d and 7f), whereas the Y(mbp)₃ inhibitors displayed a different behavior to block the pores through the formation of nodular precipitates (Fig. 7h and i). The blocking of pores retarded electrolyte penetration and thus enhanced coating barrier properties, which corresponded to the restoration of the impedance modulus and phase angle spectra (Fig. 2). The difference of inhibiting behavior between La(4-OHcin)₃ and Y(mbp)₃ compounds is possibly related to their different solubility, speciation, and interaction with electrolyte and coating matrix.

3.2.3. Mild steel surface

The following SEM/EDS analysis of corrosion products was carried out on the mild steel surface after coating removal. Fig. 8a and b show that apparently localized corrosion occurred on the mild steel surface underneath the control coating. Pits and filaments were observed on the metal surface and shown in Fig. 8c and d, respectively. EDS spectrum (Fig. 8e) shows the presence of S from the corrosion products formed on the pitting area (site A), suggesting that the pits might initiate at MnS inclusions of mild steel [45]. The detection of Cl on the pitting spots (site A) and the filaments (site B) confirms the penetration of electrolyte to

the coating/metal interface. Considerably higher amount of O was detected from the corroded area (site A and site B) compared to that of the surrounding metal surface (site C), implying the formation of localized iron-based corrosion products beneath the control coating.

Only one stained region with a cap-like structure was observed on the mild steel surface underneath the 10 wt% of La(4-OHcin)₃ loaded coating, as shown in Fig. 8f and g. A similar cap structure was reported for the metal surface immersed in solutions containing dissolved rare earth carboxylate compounds [15]. The cap-like structure was partially damaged, which might result from the coating removal and dehydration process. Apparent polishing scratches (Fig. 8h) and various lumps (Fig. 8i) were observed on the surface of the cap structure. These features were absent from the control specimen. However, EDS analysis (Fig. 8j) shows that La was not detected from the areas with polishing marks (site A) and the lumps (site B) on the cap structure. SEM and EDS analysis suggests that a more robust protective layer rather than loose corrosion products was formed on the mild steel surface under La(4-OHcin)₃ containing coatings.

Filiform corrosion, a type of corrosion commonly occurs on the metal substrate beneath coatings, was observed on the rusted area of the metal surface under the Y(mbp)₃ modified coating, as shown in Fig. 8k and l. The features observed from the other two specimens, such as the pits and the lumps, were absent from the mild steel surface underneath the Y(mbp)₃ loaded coatings. The center and the edge of the filaments were magnified and shown in Fig. 8m and n, respectively. The EDS spectrum (Fig. 8o) shows that no Y was detected on the metal surface (site A) and the filaments (site B), while Cl was present in the filiform corrosion products.

The metal surfaces under the coatings containing inhibitor compounds were much less damaged as no pitting was observed compared to the control coating. However, rare earth elements were not detected from the products formed on the metal surfaces, which might be due to the concentration of inhibitor species in the oxide layer being below the EDS detection limit.

3.3. Filiform corrosion tests

3.3.1. Optical images

Previous EIS experiments and SEM/EDS analysis of the polymeric matrix and the metal surface for each coating system with and without inhibitors determine the long-term corrosion protection performance of rare earth carboxylate compounds in an intact coating. Thereafter, filiform corrosion tests were applied to investigate the active corrosion protection provided by the released rare earth carboxylate inhibitors to the mild steel surface exposed to a scribed coating defect. The optical images were taken every 2–3 days to monitor the initiation and development of filiform corrosion along the coating defect. In this paper, the coated samples containing 0, 10, and 20 wt% of La(4-OHcin)₃ or Y(mbp)₃ inhibitors after 0, 3, 7, 14, 21, and 30 days exposure to the filiform corrosion testing environment were chosen to compare and examine their active corrosion inhibiting performance.

Fig. 9 shows the development of filaments and the delamination of coatings along the scribe with exposure time increased for the control and the inhibited specimens. Within the initial 3 days of experiments, all the coated samples exhibited some extent of discoloration in the activated scribe, suggesting the formation of rusts on the exposed mild steel surface. The coating delamination and thick filaments were only observed on the control specimen after 3 days exposure, while these features were nearly negligible for the coated samples containing inhibitors. After 7 days of filiform corrosion tests, the control sample shows a rapid increase of the filament length and the delamination area. For the coating loaded with 10 wt% of inhibitors, the number and the length of the filaments gradually increased between 3 and 7 days of exposure. In contrast, the generation of filaments was significantly stifled by the coated specimens containing 20 wt% of inhibitors. With the exposure time further prolonged, the control coating and the 10 wt% of

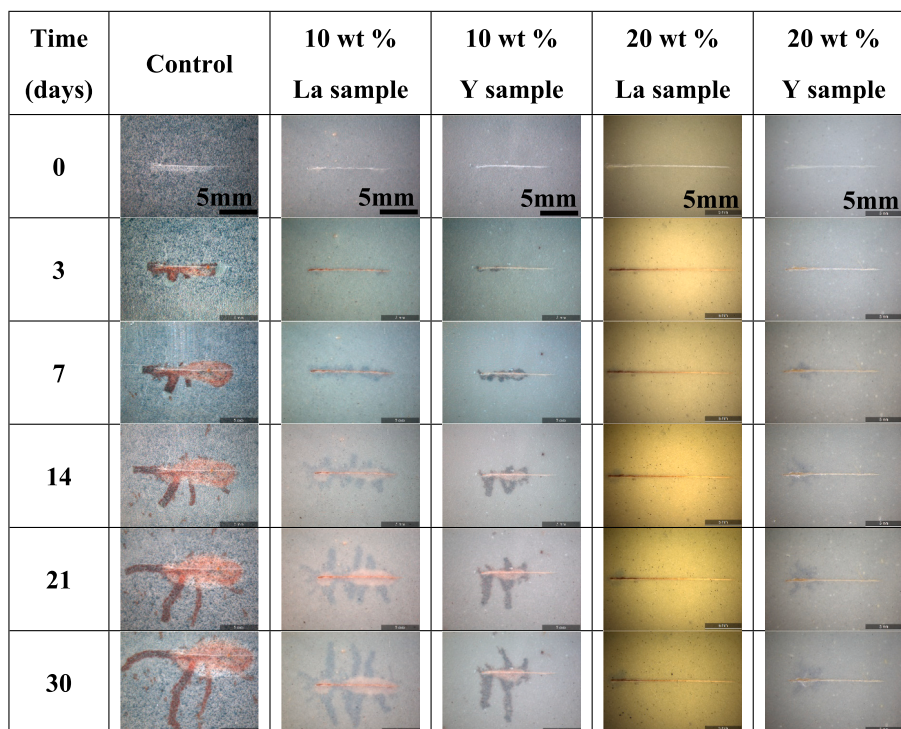


Fig. 9. The growth of filiform corrosion with exposure time on mild steel surface underneath the control coating without inhibitors and the inhibited coatings containing 10 and 20 wt% of $\text{La}(\text{4-OHcin})_3$ or $\text{Y}(\text{mbp})_3$ particles.

inhibitor loaded coatings displayed a very limited capability to mitigate filiform corrosion, as the length of filament and the area of delamination were exacerbated significantly. The inhibiting performance was substantially improved by increasing the loading of rare earth carboxylates. For the coating system incorporated with 20 wt% of inhibitors, no delamination was observed and the growth of filaments was considerably retarded. The coated specimen containing 20 wt% $\text{La}(\text{4-OHcin})_3$ particles shows the best performance for the protection of filiform corrosion, which effectively curbed the initiation and development of the filaments and coating delamination.

3.3.2. SEM/EDS analysis of the artificially scratched area

After filiform corrosion tests, all the coated samples were immersed in acetone to soften and remove the coatings for the observation of bare mild steel surfaces (optical images for bare metal panels were shown in Fig. S8 in SI) [26]. SEM and EDS were employed to observe the surface morphology near the artificial scribe and analyze the possible distribution of rare earth elements. The filaments with various shapes, length, and thickness are presented in Fig. S9 in SI. EDS results show that the filaments predominantly consisted of Fe and O, and a Cl rich region was only found at the head of the filament, while no rare earth elements were detected on the bulk filaments.

The control sample shows that the entire scribe was covered by loosely distributed corrosion products with porous surface morphology, as presented in Fig. 10a and b. The build-up of corrosion products surrounding the scribe caused coating delamination at the metal/coating interface. Fig. 10c shows that the porous surface structure (site A in Fig. 10b) predominantly comprised of Fe and O i.e., the Fe corrosion products. The scribe next to the coating containing 10 wt% of $\text{La}(\text{4-OHcin})_3$ inhibitors was partially covered by amorphous corrosion products (Fig. 10d and e), contributing to a less rough metal surface compared to the control specimen. EDS analysis (Fig. 10f) confirms the presence of La in the surface layer formed on the scribe (site A in Fig. 10d and site B in Fig. 10e), suggesting the corrosion protection of the metal substrate against chloride attack provided by the released $\text{La}(\text{4-OHcin})_3$ species in coatings. A relatively smooth surface film was formed on the

scribed defect beneath the 10 wt% of $\text{Y}(\text{mbp})_3$ loaded coating specimen, as shown in Fig. 10g and h. The detection of Fe, Y, and O in the surface film (EDS spectra shown in Fig. 10i for site A (Fig. 10g) and site B (Fig. 10h), respectively) indicates the deposition of a mixture of Fe and Y oxides/hydroxides in the defect. After removal of the coating loaded with 20 wt% of $\text{La}(\text{4-OHcin})_3$, it can be seen that the mild steel surface was covered by a thin and compact film with polishing lines observed underneath, as shown in Fig. 10j and k. Fig. 10j shows that numerous loosely arranged precipitates were formed on the thin surface film, and La was detected from the surface particles (see EDS spectrum of site A shown in Fig. 10l). Fig. 10k shows that the scribe was covered by protuberant corrosion products, generating a continuous and ridge-shaped appearance, which was surrounded by the compact surface layer. EDS analysis (Fig. 10l) confirms the presence of La on the ridge structure (site B in Fig. 10k) and the peripheral surface film (site C in Fig. 10k). Fig. 10m and n exhibit the surface morphology of the scribed metal substrate after peeling off the coating containing 20 wt% of $\text{Y}(\text{mbp})_3$ inhibitors. A dense arrangement of precipitates was observed on the metal surface adjacent to the scribe, as shown in Fig. 10m. Also, Fig. 10n shows the deposition of ridge-like protuberance on the scribed defect, surrounding by a compact surface film. EDS results show that Y was widely distributed in the vicinity of the scribed area (Fig. 10o), such as on the precipitate (site A in Fig. 10m), the ridge structure (site B in Fig. 10n) and the nearby surface film (site C in Fig. 10n), indicating the active corrosion protection provided by the released inhibitor species.

The investigation of mild steel surfaces after filiform corrosion tests confirms that all the inhibitor containing coatings provided some extent of corrosion protection to the scribed defect. The protective layer was generated on top of the metal at the damaged site through the interaction between the released inhibitors and the mild steel substrate. By increasing the inhibitor loading from 10 to 20 wt%, the protective layer became thicker and more compact, and the coverage also extended further to the area in the vicinity of the scribe. Moreover, the scribed defect was not visible and completely covered by the protective layer, implying the self-healing effect provided by the released inhibitors to the mild steel surface exposed to corrosive environment. The active

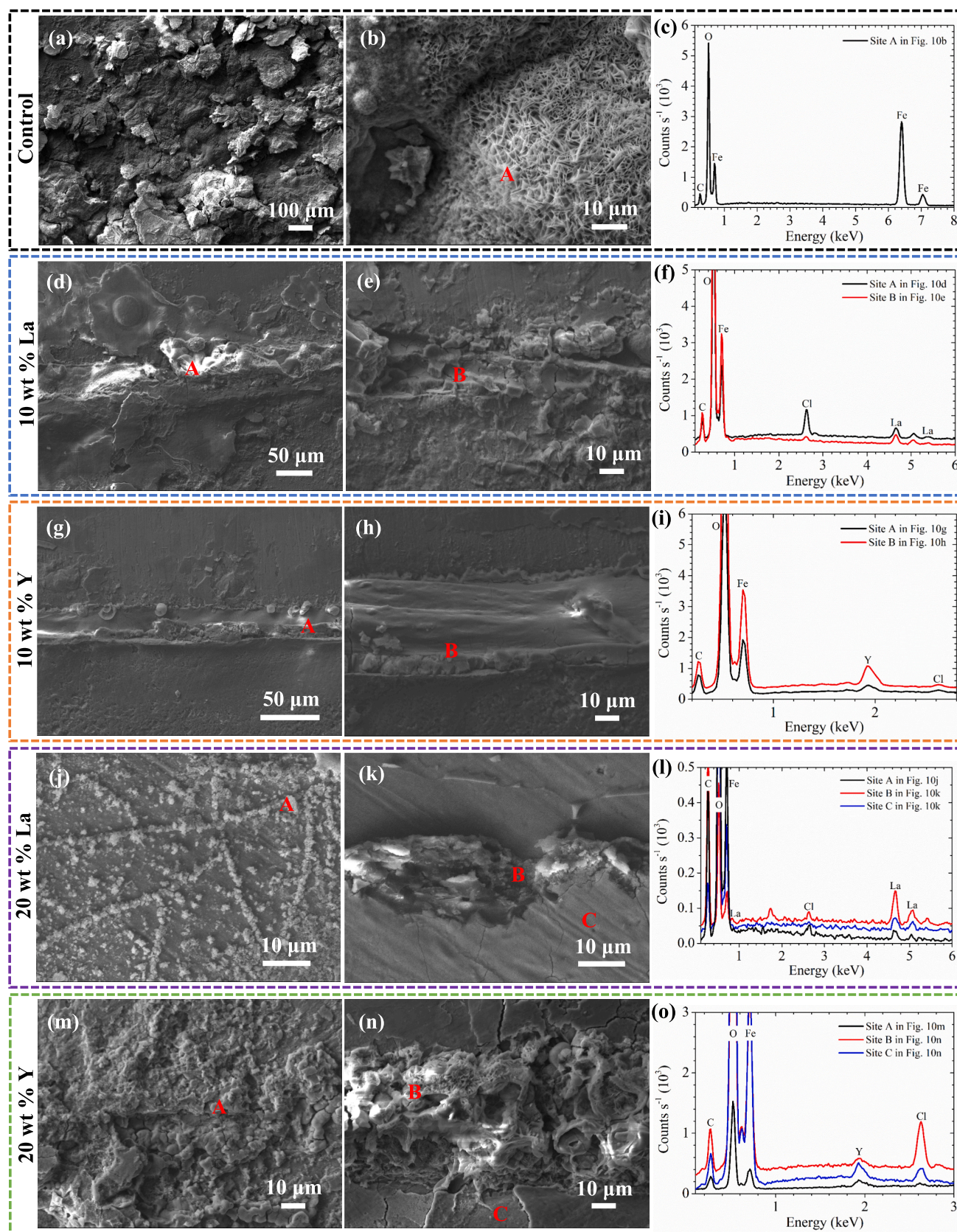


Fig. 10. SEM and EDS analysis for the scribed area underneath (a)–(c) the control coating without inhibitors; (d)–(f) the coating loaded with 10 wt% of $\text{La}(\text{4-OHcin})_3$ powders; (g)–(i) the coating modified with 10 wt% of $\text{Y}(\text{mbp})_3$ powders; (j)–(l) the coating incorporated with 20 wt% of $\text{La}(\text{4-OHcin})_3$ powders; (m)–(o) the coating containing 20 wt% of $\text{Y}(\text{mbp})_3$ powders.

inhibition behavior can be inferred from the widely distributed rare earth elements in the surface protective layer. This rare earth containing protective layer was thought to fill in the defect and prevent the continuous infiltration of corrodents to the metal substrate, thus effectively stifling the development of filiform corrosion.

3.3.3. SEM/EDS analysis for underfilm corrosion

The cross-section of each metal panel was produced perpendicular to the scribe for the purpose of assessing the subsurface damage.

Fig. 11a shows the cross-sectioned surface of the control sample, where the entrapped bright particles are SiC residues from polishing papers, the dark region represents the mounting epoxy, the bottom grey region is the mild steel substrate, and the grey layer at the mounting epoxy/mild steel interface represents the subsurface corrosion products. The control metal panel exhibits a relatively even distribution of corrosion products at the fractured surface, with a penetration depth lower than 10 μm .

The sectioned mild steel panels show a deeper and more localized underfilm attacks for the 10 wt% of inhibitor loaded specimens (Fig. 11c and e), in particular, the penetration depth of the La(4-OHcin)₃ containing sample significantly increased to approximately 40 μm . This phenomenon was most likely related to an insufficient concentration of the released La(4-OHcin)₃ species, resulting in the acceleration of corrosion process by anodic inhibitors [46]. Therefore, the areas that were not protected suffered severe corrosion attack. In contrast, the subsurface attacks were considerably suppressed by the coated specimens containing 20 wt% of inhibitors (Fig. 11g and i), as the penetration depth of corrosion damage under the mild steel surface was estimated to be only a few microns. The cross-sectional analyses of the mild steel panels show that rare earth elements were not detected from the subsurface layer (EDS spectra for site A-E are displayed in Fig. 11b, d, f, h, and j). The results were different compared to the planar observations (shown in Fig. 10) that rare earth containing products were widely distributed on the metal surface. This suggests that the underfilm region created by sectioning is difficult to intercept a rare earth-containing particle.

4. Discussion

This work has examined the long-term corrosion protection performance provided by rare earth carboxylate compounds (La(4-OHcin)₃ and Y(mbp)₃) incorporated in epoxy coating systems. Based on the long-term electrochemical measurements, both rare earth carboxylate loaded coatings exhibit enhanced corrosion resistance and coating barrier properties in comparison with the control coating without inhibitors. This was also confirmed using the breakpoint frequency method and equivalent circuit modelling. The results of filiform corrosion tests proved active corrosion inhibition provided by the leached rare earth containing species for mild steel exposed to the coating defect. The effects of rare earth carboxylates on coating barrier properties and their active inhibition on metal surfaces were discussed.

4.1. Coating barrier properties

The La(4-OHcin)₃ inhibited coating exhibits a more obvious pore-plugging effect compared to the coating loaded with Y(mbp)₃. This phenomenon could be caused by different leaching behavior and inhibitor-coating interactions between the two rare earth carboxylates. Previous work on leaching of rare earth carboxylates from epoxy coating suggests that leaching occurs at the coating/solution interface, where inhibitor is depleted through the top surface of the coating, creating a depletion zone with pores [24]. The water-uptake also swells the coating causing more pathways within the coating system [47]. For the epoxy coating with the same inhibitor loading level, a faster leaching rate is achieved by La(4-OHcin)₃ than Y(mbp)₃, in particular, at lower pH condition. The water-uptake process and the dissolution of inhibitors

result in the formation of conductive pathways along the pore/electrolyte interface. The species migrating through the conductive pathways include H₂O, O₂, OH⁻, inhibitor ions, metal ions and counterions, creating a complex chemical environment in the pores [48]. The changing chemical environment may trigger the release of inhibitor species at the pore/electrolyte interface, which will precipitate out when solubility product exceeded. Therefore, the insoluble La containing precipitation blocks the coating pores and the conductive pathways, contributing to improve the coating barrier properties. This is consistent with the detection of strong signal intensity of La in the half-blocked pores.

Y(mbp)₃ shows a different behavior in the coating compared to La(4-OHcin)₃, possibly affected by their differences in stability, solubility, leaching behavior, and speciation. According to previous work on rare earth metal compounds, the smaller the ionic radius of the rare earth metals, the more stable are their complexes [14]. Y³⁺ has a smaller ionic radius in comparison with La³⁺, thus the Y complexes should obtain a better stability in solution [49]. It is known that greater inhibition efficacy will be obtained for rare earth carboxylate which remained as a complex, rather than separating into individual rare earth cation and organic anion components [11]. Moreover, the maximum solubility in NaCl solution for Y(mbp)₃ is around 0.25 mM, while the solubility limit reaches up to approximately 1.1 mM for La(4-OHcin)₃. The slower leaching rate and the limited solubility as well as the good stability of the Y(mbp)₃ complex leads to the retention of most Y(mbp)₃ compounds in coatings, even in a very acidic environment [24]. These features contribute to enhance the coating barrier properties and the corrosion resistance at metal/coating interface for the Y(mbp)₃ loaded coating on mild steel, which can be inferred from its highest overall impedance and the almost pristine metal surface. Intriguingly, a unique nodular-like deposit was formed on the sectioned surface of the coating containing Y(mbp)₃. The presence of the nodular structure means that gel-like species exist within the coating, which were dried and precipitated in vacuum condition. The nodules were observed as part of the background film, which was generated on a mild steel surface immersed in NaCl solution with dissolved Y(mbp)₃ [14]. The evidence from the NMR data for a series of [RE(mbp)₃(H₂O)] complexes shows that carboxylate coordination persists in solution [29]. This is indicative that the dissolved Y(mbp)₃ species tend to remain as a complex, achieving greater stability in solution. EDS data show that the nodule contained a great amount of Y with C and O. Much less Cl and Na were also detected, but Fe was absent. Consequently, the reaction between the released Y(mbp)₃ species and the infiltrated NaCl electrolyte determines the speciation and composition of the products in coating pores, leading to a distinctive behavior to reinforce the coating barrier properties.

4.2. Active inhibition on metal surface

The 10 wt% of rare earth carboxylate loaded coatings show that the amorphous corrosion product was formed in the slot, which was surrounded by the remnants of filaments. The protection of this layer was limited and seems unable to extend to the nearby metal surface, and thus was not capable of curbing filiform corrosion with time, resulting in a deeply rough and rusted surface morphology on the metal substrate. The inhibition of filiform corrosion was enhanced pronouncedly by coatings loaded with 20 wt% of rare earth carboxylates, possibly attributed to greater leaching rate of the inhibitors and their reactions on mild steel surfaces. The active protection for the slot and the adjacent area relies on the interaction between the dissolved and leached inhibitor species and the mild steel surface. Therefore, the reaction and speciation at the metal/coating interface can be referred to previous corrosion studies in solutions containing dissolved rare earth carboxylates. It is assumed that at acidic pH and low inhibitor concentrations, the active rare earth carboxylate species is likely to be identical to [RECl₄]⁻ ions (RE = La or Y), while with the inhibitor concentration increases more organic ligands are included in speciation ([RELCl₃]⁻, [REL₂Cl₂]⁻, [REL₃Cl]⁻,

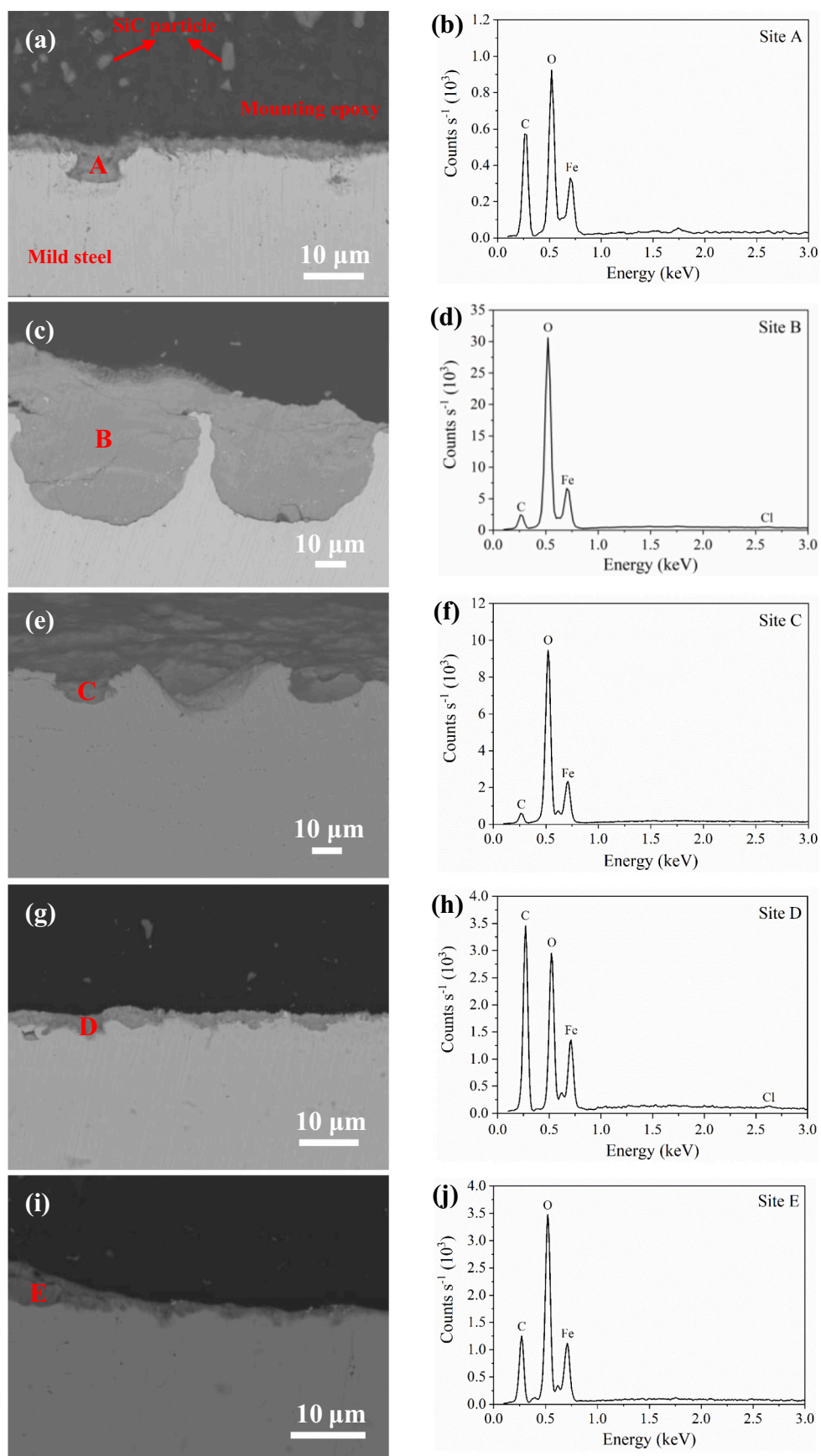


Fig. 11. SEM images and EDS spectra for the cross-sectioned surfaces of the mild steel panels after removal of coatings without inhibitors (a and b), and the coating loaded with 10 wt% of La(4-OHcin)_3 (c and d), 10 wt% of Y(mbp)_3 (e and f), 20 wt% of La(4-OHcin)_3 (g and h), and 20 wt% of Y(mbp)_3 (i and j).

and $[\text{REL}_4]^-$; $L = [4\text{-OHcin}]$ or $[\text{mbp}]$, shifting the inhibition behavior from cathodic to mixed inhibition [11]. Considering the initial exposure of the slot to very acidic conditions, the local concentration of inhibitors in the slot will be significantly higher for the 20 wt% of inhibitor loaded coatings compared to their 10 wt% counterparts because of the higher leaching rates, contributing to the suppression of both the anodic and the cathodic corrosion reactions at the early stage. The coated specimens were then transferred to a humid chamber with saturated KCl solutions. This causes the change of the localized pH in the slot. It is proposed that at neutral and basic pH the rare earth carboxylate complexes are favored in solutions, and can readily bond to the mild steel surface and react with the underlying iron or iron oxide to form bimetallic complexes, hence generating a surface protective layer [11]. Also, rare earth metals commonly prefer coordination numbers 8–10 and may form species with polymeric-like structure [49]. If these species deposit from solution and attach to the metal substrate underneath in a polymeric form, they will then prompt the extension of the surface protective film [14]. This is consistent with the observation that the coverage of the surface protective layer increased, from which rare earth metals were universally detected (Fig. 10j–o).

The FTIR data show a shift in the $\text{C}=\text{C}$ and $\text{C}=\text{O}$ as well as the COO^- stretching vibrations on the metal surface in comparison with the parent inhibitors, which suggests that both the 4-OHcin and mbp groups are bound differently in the surface film [14,50]. This implies bonding to the metal surface rather than just precipitation of the unchanged inhibitor complex on the surface. These studies confirm the presence of an organic component containing film on the mild steel surface that only occurred when the rare earth was present. The rare earth cinnamate and rare earth substituted cinnamate compounds are bound to the mild steel surface through a bridging or chelating bridging and/or other bonding modes [50]. The carboxylate group of the mbp ligand may bind to iron oxide surface by bridging bidentate coordination bonds, while its carbonyl group interacts with the surface hydroxyl groups by hydrogen binding, suggesting a bifunctional mode of bonding of the mbp ligand to the underlying metal substrate [17,18].

For the rare earth carboxylate incorporated coating systems, the capacity of active corrosion inhibition links to the fast and continuous leaching of inhibitors from coatings and their subsequent interaction with the underlying mild steel surface. The rapid leaching behavior guarantees sufficient local concentration of inhibitors mitigating anodic metal dissolution by forming a surface protective film, combining the iron of the metal substrate with the organic carboxylate moiety of the inhibitor complex, typically forming a bimetallic Fe-carboxylate-rare earth metal surface film [6]. This quick and active response slows the anodic reactions at the filament tip and restricts the formation of new anodic sites that allow for filament propagation [21]. However, in the initial stage, the surface protective film might be thin and/or conductive enough to still allow oxygen and electrons as well as transport of ions to the cathodic sites [19], which leads to the change of the localized pH to alkaline conditions as the cathodic reaction continues. The increase in local alkalinity causes the breakage of rare earth metal-carboxylate coordination bonds and the hydrolysis of the rare earth metal ions, leading to the precipitation of rare earth metal hydroxide and iron oxide/hydroxide species on the mild steel surface due to their solubility being exceeded at higher pH conditions. The mixed precipitates make it harder for oxygen and ion migration to the cathode [51]. Since oxygen is the driving force for filiform corrosion [52,53]. This explains why the growth of filament length and number as well as the development of the delamination front were effectively stifled for the coating loaded with higher amount of inhibitors. Subsequently, slower but continuous replenishment as the rare earth carboxylate compounds leach out, would contribute to the extension and densification of this surface protective film. This is consistent with the observation that a layer of ridge-shaped precipitates in a dense arrangement on the scribe occurred and a uniform and compact layer formed in close proximity to the scribe. Therefore, the mild steel substrate will be covered by a surface

protective film consisting of bimetallic complexes and a mixture of rare earth metal and iron oxide/hydroxide precipitates. This is indicative of a self-healing ability provided by the released rare earth carboxylate species on a mild steel surface, that actively prohibits both the anodic metal dissolution process and the cathodic oxygen reduction reaction. Generally, both the $\text{La}(4\text{-OHcin})_3$ and $\text{Y}(\text{mbp})_3$ follow the above inhibition mechanism and their effectiveness of active inhibition is affected by multiple factors, such as leaching rate, transport pathway, solubility limit, speciation, and interactions between the metal substrate and the inhibitor species.

5. Conclusions

This study represents a further step toward evaluating rare earth carboxylate incorporated coating systems via long-term EIS monitoring and filiform corrosion experiments. The results presented here clearly indicate the dual function of rare earth carboxylate species on the coating barrier properties and active inhibition ability.

Based on the EIS data and surface characterization of the coating matrix and the metal substrate, it is clear that the rare earth carboxylate incorporated coating exhibits greatly enhanced effectiveness in corrosion protection performance on mild steel relative to controls. The electrochemical responses show that the coatings containing inhibitors obtain a higher global impedance modulus and broader phase angle plateau as well as the absence of middle frequency time constant in comparison with the control specimen. These phenomena are consistent with the results from the breakpoint frequency method and equivalent circuit modelling. Moreover, EIS spectra for the coating with inhibitors constantly show a decline and restoration process, implying the leaching and precipitation of inhibitor species in coating pores, resulting in the formation of half-blocked pores by precipitates containing rare earth compounds. This pore-plugging behavior effectively barricades against electrolyte diffusion into the bulk of the coating, thus playing a paramount role for the improvement of coating barrier properties.

Another notable feature of rare earth carboxylate loaded coatings is their active corrosion inhibition. The self-healing ability of artificially scratched coatings, observed by filiform corrosion experiments, arises from the interaction between the leached rare earth carboxylate species and the adjacent corrosion spots by formation of a surface protective film within and adjacent to the scratch track. This film consists of bimetallic complexes with the organic ligands and a mixture of rare earth metal and iron oxide/hydroxide precipitates. The formation of insoluble hydroxides driven by lanthanide compounds enables the cathodic inhibition process. It was found that higher inhibitor loadings promote active corrosion inhibition, thus efficiently stifling the initiation and growth of filaments along with the development of any delamination front. The high mobility and chemical activity of $\text{La}(4\text{-OHcin})_3$ and $\text{Y}(\text{mbp})_3$ species may be the driving force for the observed active inhibition process.

Hence, it can be concluded that rare earth carboxylate inhibitors possess a dual role in the coating system, that is to reinforce the coating barrier properties against corrosive species and to provide active corrosion inhibition on mild steel by creating a bimetallic complex surface film with a mixture of precipitates. It is worth noting that EDS is difficult to detect rare earth species when their concentration is below the detection limit. Therefore, in the future work, more sensitive surface characterization methods (such as XPS) will be applied to investigate the interaction between the rare earth species and the metal surface to gain insights into the mechanism of protection provided by the rare earth carboxylate inhibitors at the metal/coating interface.

CRedit authorship contribution statement

Yu Peng: Conceptualization, Methodology, Validation, Formal analysis, Investigation, Data curation, Writing – original draft.

Anthony E. Hughes: Supervision, Conceptualization, Writing –

review & editing.

James I. Mardel: Supervision, Writing – review & editing.

Glen B. Deacon: Resources – supply of inhibitors, Writing – review & editing.

Peter C. Junk: Resources – supply of inhibitors, Writing – review & editing.

Rainier A. Catubig: Writing – review & editing.

Maria Forsyth: Supervision, Conceptualization, Project administration, Funding acquisition, Writing – review & editing.

Bruce R. W. Hinton: Conceptualization, Writing – review & editing.

Anthony E. Somers: Supervision, Conceptualization, Project administration, Funding acquisition, Writing – review & editing.

Declaration of competing interest

The authors declare that they have no known competing financial interests or personal relationships that could have appeared to influence the work reported in this paper.

Data availability

Data will be made available on request.

Acknowledgments

AS is grateful to Deakin University for funding his Alfred Deakin Postdoctoral Research Fellowship. AS and MF are grateful for funding from the Australian Research Council through a Discovery Project (Grant No. DP180101465). GD and PJ are grateful for initial funding from The ARC Centre for Green Chemistry and are grateful for funding from the Australian Research Council through a Discovery Project (Grant No. DP200100568). YP is grateful for initial funding from Deakin University Postgraduate Research (DUPR) scholarships and for funding from the Knowledge Innovation Program of Wuhan-Shuguang Project (Grant No. 2022010801020374). We would like to acknowledge Ruhamah Yunis and Yuqing Tan for the synthesis of corrosion inhibitors used in this study and to thank John Ward for the access to the microtome and the carbon coater.

Appendix A. Supplementary data

Supplementary data to this article can be found online at <https://doi.org/10.1016/j.porgcoat.2023.107870>.

References

- O. Gharbi, S. Thomas, C. Smith, N. Birbilis, Chromate replacement: what does the future hold? *Npj Mater. Degrad.* 2 (2018) 23–25.
- Y.F. Wang, H. Su, Y.L. Gu, X. Song, J.S. Zhao, Carcinogenicity of chromium and chemoprevention: a brief update, *OncoTargets Ther.* 10 (2017) 4065–4079.
- C. Pellerin, S.M. Booker, Reflections on hexavalent chromium - health hazards of an industrial heavyweight, *Environ. Health Perspect.* 108 (2000) A402–A407.
- B.R.W. Hinton, L. Wilson, The corrosion inhibition of zinc with cerous chloride, *Corros. Sci.* 29 (1989) 967–985.
- B.R.W. Hinton, The inhibition of aluminum alloy corrosion by cerous cations, *Met. Forum* 7 (1984) 211–217.
- M. Forsyth, M. Seter, B. Hinton, G. Deacon, P. Junk, New “green” corrosion inhibitors based on rare earth compounds, *Aust. J. Chem.* 64 (2011) 812–819.
- M. Forsyth, K. Wilson, T. Behrsing, C. Forsyth, G.B. Deacon, A. Phanasoankar, Effectiveness of rare-earth metal compounds as corrosion inhibitors for steel, *Corrosion* 58 (2002) 953–960.
- M. Forsyth, C.M. Forsyth, K. Wilson, T. Behrsing, G.B. Deacon, ATR characterisation of synergistic corrosion inhibition of mild steel surfaces by cerium salicylate, *Corros. Sci.* 44 (2002) 2651–2656.
- F. Blin, S.G. Leary, K. Wilson, G.B. Deacon, P.C. Junk, M. Forsyth, Corrosion mitigation of mild steel by new rare earth cinnamate compounds, *J. Appl. Electrochem.* 34 (2004) 591–599.
- F. Blin, P. Koutsoukos, P. Klepatsianis, M. Forsyth, The corrosion inhibition mechanism of new rare earth cinnamate compounds - electrochemical studies, *Electrochim. Acta* 52 (2007) 6212–6220.
- M. Seter, B. Hinton, M. Forsyth, Understanding speciation of lanthanum 4-hydroxy cinnamate and its impact on the corrosion inhibition mechanism for AS1020 steel, *J. Electrochem. Soc.* 159 (2012) C181–C189.
- N.D. Nam, C. Panaitescu, M.Y.J. Tan, M. Forsyth, B. Hinton, An interaction between praseodymium 4-hydroxycinnamate with AS1020 and X65 steel microstructures in carbon dioxide environment, *J. Electrochem. Soc.* 165 (2018) 50–59.
- T.D. Manh, P.V. Hien, Q.B. Nguyen, T.N. Quyen, B.R.W. Hinton, N.D. Nam, Corrosion inhibition of steel in naturally-aerated chloride solution by rare-earth 4-hydroxycinnamate compound, *J. Taiwan Inst. Chem. Eng.* 103 (2019) 177–189.
- A.E. Somers, B.R.W. Hinton, C. de Bruin-Dickason, G.B. Deacon, P.C. Junk, M. Forsyth, New, environmentally friendly, rare earth carboxylate corrosion inhibitors for mild steel, *Corros. Sci.* 139 (2018) 430–437.
- Y. Peng, A.E. Hughes, G.B. Deacon, P.C. Junk, B.R.W. Hinton, M. Forsyth, J. I. Mardel, A.E. Somers, A study of rare-earth 3-(4-methylbenzoyl)-propanoate compounds as corrosion inhibitors for AS1020 mild steel in NaCl solutions, *Corros. Sci.* 145 (2018) 199–211.
- G.B. Deacon, P.C. Junk, W.W. Lee, M. Forsyth, J. Wang, Rare earth 3-(4'-hydroxyphenyl)propionate complexes, *New J. Chem.* 39 (2015) 7688–7695.
- M. Frey, S.G. Harris, J.M. Holmes, D.A. Nation, S. Parsons, P.A. Tasker, R.E. P. Wimpenny, Elucidating the mode of action of a corrosion inhibitor for iron, *Chem. Eur. J.* 6 (2000) 1407–1415.
- M. Frey, S.G. Harris, J.M. Holmes, D.A. Nation, S. Parsons, P.A. Tasker, S.J. Teat, R. E.P. Wimpenny, Modeling surface engineering: use of polymetallic iron cages and computer graphics to understand the mode of action of a corrosion inhibitor, *Angew. Chem. Int. Ed.* 37 (1998) 3245–3248.
- A.E. Somers, Y. Peng, A.L. Chong, M. Forsyth, D.R. MacFarlane, G.B. Deacon, A. E. Hughes, B.R.W. Hinton, J.I. Mardel, P.C. Junk, Advances in the development of rare earth metal and carboxylate compounds as corrosion inhibitors for steel, *Corros. Eng. Sci. Technol.* 55 (2020) 311–321.
- A.E. Somers, G.B. Deacon, B.R.W. Hinton, D.R. MacFarlane, P.C. Junk, M.Y.J. Tan, M. Forsyth, Recent developments in environment-friendly corrosion inhibitors for mild steel, *J. Indian Inst. Sci.* 96 (2016) 285–292.
- R. Catubig, M. Seter, W. Neil, M. Forsyth, B. Hinton, Effects of corrosion inhibiting pigment lanthanum 4-hydroxy cinnamate on the filiform corrosion of coated steel, *J. Electrochem. Soc.* 158 (2011) C353–C358.
- A. Suárez Vega, C. Agustín-Sáenz, L.A. O'Dell, F. Brusciotti, A. Somers, M. Forsyth, Properties of hybrid sol-gel coatings with the incorporation of lanthanum 4-hydroxy cinnamate as corrosion inhibitor on carbon steel with different surface finishes, *Appl. Surf. Sci.* 561 (2021), 149881.
- A. Suarez Vega, C. Agustín-Sáenz, F. Brusciotti, A. Somers, M. Forsyth, Effect of lanthanum 4-hydroxy cinnamate on the polymerisation, condensation and thermal stability of hybrid sol-gel formulations, *J. Sol-Gel Sci. Technol.* 96 (2020) 91–107.
- Y. Peng, A.E. Hughes, J.I. Mardel, G.B. Deacon, P.C. Junk, M. Forsyth, B.R. W. Hinton, A.E. Somers, Leaching behavior and corrosion inhibition of a rare earth carboxylate incorporated epoxy coating system, *ACS Appl. Mater. Interfaces* 11 (2019) 36154–36168.
- M. Bethencourt, F.J. Botana, J.J. Calvino, M. Marcos, M.A. Rodríguez-Chacon, Lanthanide compounds as environmentally-friendly corrosion inhibitors of aluminium alloys: a review, *Corros. Sci.* 40 (1998) 1803–1819.
- T.H. Hu, H.W. Shi, S.H. Fan, F.C. Liu, E.H. Han, Cerium tartrate as a pigment in epoxy coatings for corrosion protection of AA 2024-T3, *Prog. Org. Coat.* 105 (2017) 123–131.
- T.H. Hu, H.W. Shi, T. Wei, S.H. Fan, F.C. Liu, E.H. Han, Corrosion protection of AA2024-T3 by cerium malate and cerium malate-doped sol-gel coatings, *Acta Metall. Sin. Engl. Lett.* 32 (2019) 913–924.
- G.B. Deacon, M. Forsyth, P.C. Junk, S.G. Leary, W.W. Lee, Synthesis and characterisation of rare earth complexes supported by para-substituted cinnamate ligands, *Z. Anorg. Allg. Chem.* 635 (2009) 833–839.
- C.N. de Bruin-Dickason, G.B. Deacon, C.M. Forsyth, S. Hanf, O.B. Heilmann, B.R. W. Hinton, P.C. Junk, A.E. Somers, Y.Q. Tan, D.R. Turner, Synthesis and structures of rare earth 3-(4'-methylbenzoyl)-propanoate complexes - new corrosion inhibitors, *Aust. J. Chem.* 70 (2017) 478–484.
- T. Markley, Corrosion Mitigation of Aerospace Alloys Using Rare Earth Diphenyl Phosphates, Thesis (Ph.D.), Monash University, Australia, 2008.
- H.P. Hack, J.R. Scully, Defect area determination of organic coated steels in seawater using the breakpoint frequency method, *J. Electrochem. Soc.* 138 (1991) 33.
- J.R. Scully, S.T. Hensley, Lifetime prediction for organic coatings on steel and a magnesium alloy using electrochemical impedance methods, *Corrosion* 50 (1994) 705–716.
- Z.C. Feng, G.S. Frankel, Evaluation of coated Al alloy using the breakpoint frequency method, *Electrochim. Acta* 187 (2016) 605–615.
- Y. Morozov, L.M. Calado, R.A. Shakoor, R. Raj, R. Kahraman, M.G. Taryba, M. F. Montemor, Epoxy coatings modified with a new cerium phosphate inhibitor for smart corrosion protection of steel, *Corros. Sci.* 159 (2019), 108128.
- M. Izadi, T. Shahrazi, B. Ramezanzadeh, Active corrosion protection performance of an epoxy coating applied on the mild steel modified with an eco-friendly sol-gel film impregnated with green corrosion inhibitor loaded nanocontainers, *Appl. Surf. Sci.* 440 (2018) 491–505.
- S.K. Poznyak, J. Tedim, L.M. Rodrigues, A.N. Salak, M.L. Zheludkevich, L.F.P. Dick, M.G.S. Ferreira, Novel inorganic host layered double hydroxides intercalated with guest organic inhibitors for anticorrosion applications, *ACS Appl. Mater. Interfaces* 1 (2009) 2353–2362.
- P.J. Denissen, S.J. Garcia, Cerium-loaded algae exoskeletons for active corrosion protection of coated AA2024-T3, *Corros. Sci.* 128 (2017) 164–175.

- [38] F.J. Presuel-Moreno, H. Wang, M.A. Jakab, R.G. Kelly, J.R. Scully, Computational modeling of active corrosion inhibitor release from an Al-Co-Ce metallic coating - protection of exposed AA2024-T3, *J. Electrochem. Soc.* 153 (2006) B486–B498.
- [39] T.H. Muster, H. Sullivan, D. Lau, D.L.J. Alexander, N. Sherman, S.J. Garcia, T. G. Harvey, T.A. Markley, A.E. Hughes, P.A. Corrigan, A.M. Glenn, P.A. White, S. G. Hardin, J. Mardel, J.M.C. Mol, A combinatorial matrix of rare earth chloride mixtures as corrosion inhibitors of AA2024-T3: optimisation using potentiodynamic polarisation and EIS, *Electrochim. Acta* 67 (2012) 95–103.
- [40] P. Visser, M. Meeusen, Y. Gonzalez-Garcia, H. Terryn, J.M.C. Mol, Electrochemical evaluation of corrosion inhibiting layers formed in a defect from lithium-leaching organic coatings, *J. Electrochem. Soc.* 164 (2017) C396–C406.
- [41] R. Raj, Y. Morozov, L.M. Calado, M.G. Taryba, R. Kahraman, A. Shakoov, M. F. Montemor, Inhibitor loaded calcium carbonate microparticles for corrosion protection of epoxy-coated carbon steel, *Electrochim. Acta* 319 (2019) 801–812.
- [42] Y. Cheng, J. Luo, Metastable pitting of carbon steel under potentiostatic control, *J. Electrochem. Soc.* 146 (1999) 970–976.
- [43] F.H. Scholes, S.A. Furman, A.E. Hughes, A.J. Hill, F. Tuomisto, K. Saarinen, S. J. Pas, Characterization of a chromate-inhibited primer by Doppler broadening energy spectroscopy, *JCT Res.* 3 (2006) 105–108.
- [44] A.E. Hughes, A. Trinchi, F.F. Chen, Y.S. Yang, I.S. Cole, S. Sellaiyan, J. Carr, P. D. Lee, G.E. Thompson, T.Q. Xiao, The application of multiscale quasi 4D CT to the study of SrCrO₄ distributions and the development of porous networks in epoxy-based primer coatings, *Prog. Org. Coat.* 77 (2014) 1946–1956.
- [45] R.E. Melchers, I.A. Chaves, R. Jeffrey, A conceptual model for the interaction between carbon content and manganese sulphide inclusions in the short-term seawater corrosion of low carbon steel, *Metals* 6 (2016) 132.
- [46] C.G. Dariva, A.F. Galio, Corrosion inhibitors—principles, mechanisms and applications, in: *Developments in Corrosion Protection*, 2014, pp. 365–379 (Ch. 16).
- [47] S.A. Furman, F.H. Scholes, A.E. Hughes, D.N. Jamieson, C.M. Macrae, A.M. Glenn, Corrosion in artificial defects. II. Chromate reactions, *Corros. Sci.* 48 (2006) 1827–1847.
- [48] A.E. Hughes, A. Trinchi, F.F. Chen, Y.S. Yang, S. Sellaiyan, J. Carr, P.D. Lee, G. E. Thompson, T.Q. Xiao, Structure and transport in coatings from multiscale computed tomography of coatings—new perspectives for electrochemical impedance spectroscopy modeling? *Electrochim. Acta* 202 (2016) 243–252.
- [49] T. Behrsing, G.B. Deacon, P.C. Junk, The chemistry of rare earth metals, compounds, and corrosion inhibitors, in: *Rare Earth-Based Corrosion Inhibitors*, 2014, pp. 1–37 (Ch. 1).
- [50] F. Blin, S.G. Leary, G.B. Deacon, P.C. Junk, M. Forsyth, The nature of the surface film on steel treated with cerium and lanthanum cinnamate based corrosion inhibitors, *Corros. Sci.* 48 (2006) 404–419.
- [51] A. Amadeh, S.R. Allahkaram, S.R. Hosseini, H. Moradi, A. Abdolhosseini, The use of rare earth cations as corrosion inhibitors for carbon steel in aerated NaCl solution, *Anti-Corros. Methods Mater.* 55 (2008) 135–143.
- [52] R.T. Ruggeri, T.R. Beck, An analysis of mass transfer in filiform corrosion, *Corrosion* 39 (1983) 452–465.
- [53] A. Bautista, Filiform corrosion in polymer-coated metals, *Prog. Org. Coat.* 28 (1996) 49–58.